remote sensing

MDPI

Article

Bistatic Scattering from Canonical Urban and Maritime Targets: A Physical Optics Solution

Gerardo Di Martino [1], **Alessio Di Simone** [1,*], **Walter Fuscaldo** [2], **Antonio Iodice** [1], **Daniele Riccio** [1] **and Giuseppe Ruello** [1]

[1] Department of Electrical Engineering and Information Technology, University of Naples Federico II, 80125 Naples, Italy; gerardo.dimartino@unina.it (G.D.M.); iodice@unina.it (A.I.); daniele.riccio@unina.it (D.R.); ruello@unina.it (G.R.)
[2] Istituto per la Microelettronica e Microsistemi, Consiglio Nazionale delle Ricerche, 00133 Rome, Italy; walter.fuscaldo@cnr.it
* Correspondence: alessio.disimone@unina.it

Highlights

What are the main findings?

- A fully analytical GO-PO bistatic scattering model is developed for a canonical target over a lossy random rough surface (ground or sea), accounting for both single- and multiple-bounce interaction mechanisms.
- The proposed model shows satisfactory agreement with numerical simulations and measurements under different operating conditions, demonstrating its accuracy and reliability despite the simplified target geometry.

What are the implications of the main findings?

- The proposed analytical model enables efficient and accurate evaluation of bistatic radar cross-sections for urban and maritime targets (e.g., buildings and large ships), making it well suited for large-scale simulations in complex environments and for improved interpretation of bistatic remote sensing data.
- The closed-form framework can support bistatic mission planning, system design, and data analysis and interpretation, while also fostering the development of advanced retrieval methodologies for urban monitoring and maritime surveillance applications in bistatic observation geometries.

Abstract

The increasing availability of microwave bistatic remote sensing data highlights the need for reliable and computationally efficient scattering models to support data interpretation, system design, and mission planning. This is particularly relevant in urban and maritime environments, where the electromagnetic (EM) interaction between buildings and ships with the surrounding environment significantly affects the observed bistatic signatures. This paper presents a fully analytical model for EM bistatic scattering from a canonical target, represented as a parallelepiped with smooth dielectric faces located over a lossy random rough surface. The formulation is developed within the framework of the Kirchhoff Approximation and accounts for both single- and multiple-bounce scattering mechanisms arising from the mutual interaction between the target and the underlying surface. Reflections from the target walls are modeled using the Geometrical Optics solution, while scattering from the rough surface is described through the zeroth-order Physical Optics approximation. The resulting closed-form expressions provide both coherent and incoherent components of the scattered field as explicit functions of system and scene parameters. The proposed closed-form model enables fast and reliable evaluation of bistatic scattering from

Check for updates

Academic Editor: Mike Wolff

Received: 13 February 2026
Revised: 10 April 2026
Accepted: 14 April 2026
Published: 17 April 2026

https://doi.org/10.3390/rs18081219

parallelepiped-like structures, such as buildings and large ships interacting with surrounding rough surfaces. This capability is particularly beneficial for the design and optimization of bistatic remote sensing missions in urban and maritime contexts as well as the development and assessment of inversion methods and large-scale analyses. Validation against numerical simulations and experimental results available in the literature demonstrates the effectiveness of the proposed approach across different operating conditions.

Keywords: electromagnetic scattering; Kirchhoff approximation; physical optics; radar cross-section; bistatic radars

1. Introduction

Reliable evaluation of the electromagnetic (EM) scattering in complex environments, such as those depicted in Figure 1, including a parallelepiped-like target lying over a rough background surface is of key relevance in a variety of microwave remote sensing applications. Indeed, an accurate prediction of the strength of the EM field received from such a composite target can support both inversion procedures aimed at retrieving EM and/or geometric information (e.g., shape, size, location, material composition) about the illuminated object or the underlying surface, as well as the optimal design of microwave remote sensing systems. Some examples include detection and classification of ship targets using bistatic radar systems, such as Global Navigation Satellite System-Reflectometry (GNSS-R) [1] and synthetic aperture radar (SAR) [2], and extraction of building height from monostatic SAR imagery [3], as well as estimation of the depth of floods occurring in urban areas [4]. Notably, as shown in [5], building scattering signatures can also be fruitfully used to devise cross-calibration methods for heterogeneous spaceborne SAR acquisitions.

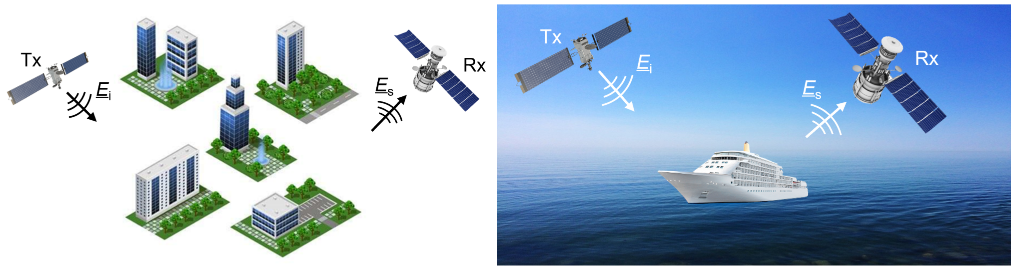

(**a**) (**b**)

Figure 1. EM scattering in complex environments: (**a**) urban scenario, (**b**) maritime scenario.

In recent decades, bistatic radar and remote sensing systems have been experiencing an increasing interest in the scientific community due to key advantages w.r.t. monostatic radars, such as the possibility to implement low-cost, low-power, and lightweight receiver-only platforms able to opportunistically acquire signals already available in the environment for remote sensing applications and technologies, e.g., passive radars and GNSS-R. Moreover, in recent years, both public space agencies and private leading companies are planning to launch innovative spaceborne SAR systems working in bistatic acquisition geometries, such as the X-band PLATiNO-1 (PLT-1) designed by the Italian Space Agency (ASI), that will form a bistatic SAR system with the COSMO-SkyMed Second Generation (CSG), also working in X band [6].

With the increasing number of bistatic microwave remote sensing systems and missions, the understanding and modeling of bistatic EM scattering is gaining increasing interest. Indeed, the modeling effort not only stands as the basis for future exploitation of bistatic radar data, but can also support the mission design phase: for instance, it could

https://doi.org/10.3390/rs18081219

support the definition of the best bistatic acquisition geometry for a specific application, thus exploiting the larger number of degrees of freedom than the monostatic case, for which the observation geometry is fixed to the backscattering one.

While evaluation of EM scattering from a rough surface (e.g., natural environments, such as bare soil, seawater, snow) is a topic of classical EM scattering theory, where numerous analytical approaches have been developed (see, e.g., classical books on the topic [7–9]), computation of EM scattering from complex targets, such as ships or buildings, has been the subject of a more limited literature, see, e.g., [10–19]. However, in most cases, the complexity of the EM interactions between the target and the ground, due to the presence of both single and multiple reflections (see Figure 2), has motivated the adoption of either statistical, fully numerical or hybrid approaches. The hybrid approaches as, for instance, the algorithms in [16–18], are typically based on the decomposition of the scene in sufficiently small facets, whose scattering is evaluated by means of analytical approaches, such as Kirchhoff Approximation (KA) or Small Perturbation Method (SPM). The overall scene scattering is then obtained by numerical integration of all the facets' contribution. Ray-tracing approaches are also typically included to determine facet EM coupling, such as multiple scattering, and shadowing regions. Finally, a Monte Carlo simulation is required to determine the received field statistics in presence of random rough surfaces. Accordingly, hybrid and full-wave techniques offer the capability to deal with arbitrarily complex target geometries, also including fine structure details, such as windows and superstructures, at a cost of a large computational cost; in addition, they cannot provide physical insights into the involved scattering mechanisms. As a matter of fact, the application of such methods for information retrieval purposes as well as for system design is rather limited due to the lack of a direct and algebraic relationship between the scene and target parameters and the radar return. Additionally, in the case of electrically large scenes, scattering evaluations based on numerical methods might require unacceptable computational time or even be unfeasible.

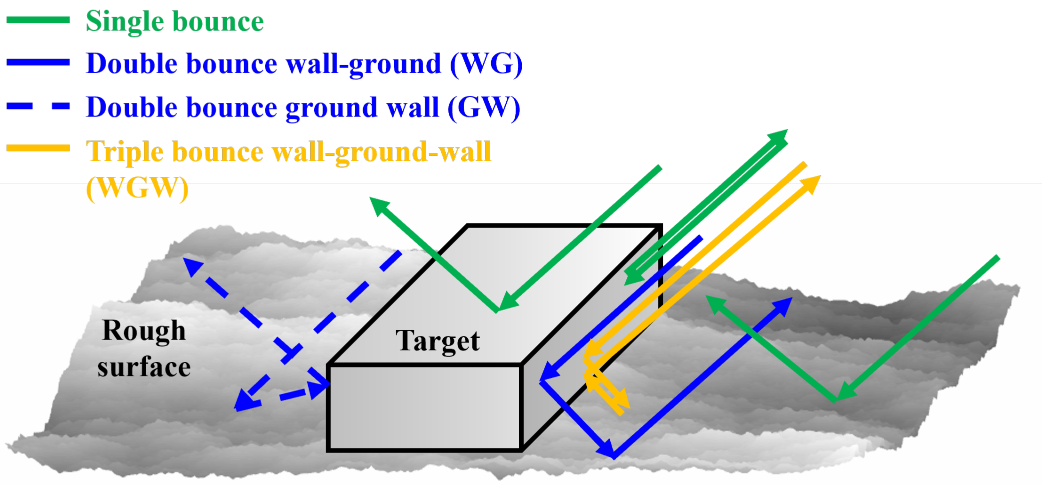

Figure 2. Scattering problem from a parallelepiped target (e.g., a building, or also, possibly, a large ship) over a rough background surface (e.g., bare soil or sea surface). The different scattering contributions are identified as follows: single-bounce from target and ground (green solid arrows), double-bounce wall–ground (WG) (blue solid arrows), double-bounce ground–wall (GW) (blue dashed arrows), and triple-bounce wall–ground–wall (WGW) (yellow solid arrows).

Conversely, analytical approaches can be applied if simplified target geometries are assumed, as done in [19–21], where closed-form evaluations of the single and multiple bounces have been derived. The primary aim of such closed-form approaches is not so much providing highly accurate radar cross-section (RCS) evaluations for specific targets, but rather to provide mathematical tools for the investigation of the main scattering mechanisms arising from the target-ground EM interaction. In [19], an analytical formulation of the so-called four-path model is presented within the framework of the first-order small-slope approximation (SSA). It can deal with an arbitrary target geometry, but the analysis is limited to the coherent component of the bistatic RCS and to isotropic rough surfaces. In [20,21], the target is modeled as a smooth parallelepiped and scattering from its vertical faces, hereafter referred to as walls, is evaluated via Geometrical Optics (GO), while ground reflections are modeled via GO and Physical Optics (PO) in [20] and the SPM in [21]. However, such works focused on isotropic ground surfaces and on backscattering evaluation only, which is of relevance for monostatic radars. Accordingly, the models in [20,21] cannot be adopted for the analysis of microwave radar systems working in bistatic or multistatic configurations. More recently, the backscattering formulation presented in [20] was generalized to the bistatic case in [22], where, however, both target and ground scattering was described by means of GO. Such a GO-GO bistatic model was further generalized to anisotropic surfaces in [23]. However, the GO solution for modeling scattering from the rough surface provides reliable results in the case of very rough surfaces (as e.g., moderate to rough sea surface), while in the case of a smooth ground (e.g., calm sea, bare soil, asphalt), the PO solution is recommended.

In this paper, we complement the GO-GO bistatic scattering model in [22] with the GO-PO formulation, where scattering from the ground is described via the PO solution, instead of the GO one, which, conversely, is still adopted for describing scattering from the smooth target walls, as done in the previous works [20–22]. Accordingly, we derive analytical expressions for the coherent and the incoherent components of the EM field scattered from a canonical parallepiped target lying over a lossy ground, modeled as a two-dimensional (2-D), possibly anisotropic, random rough surface of finite dimensions.

The proposed approach offers key features compared to hybrid/numerical approaches as well as other analytical models. First, the simplified target geometry allows for expressing efficiently the EM coupling between the object and the surrounding background surface through closed-form algebraic expressions, thus providing physical insights into the role of the different target and scene parameters mainly involved into the scattering and multiple-reflection mechanisms. Additionally, no facet decomposition, numerical integrations, Monte Carlo simulations, or measurements calibration are required by our fully analytical approach. The proposed scattering model can describe (analytically) the dependency of the field scattered from the target upon ground surface roughness conditions, including potential ground surface anisotropy, that is neglected in other analytical models, such as those in [20–22]. Finally, the SPM adopted in [21], despite being able to account for surface anisotropy, is often not accurate at near-specular scattering directions, which can be important in the mutual interaction between target and surface. Additionally, it typically exhibits a narrower validity range compared to PO.

Moving to the limitations, our analytical model is not able to catch higher-order scattering effects, such as those arising from the multiple interactions between fine structure details, such as windows and superstructures. Moreover, the adoption of the PO solution for ground surface scattering limits the applicability of our model to sufficiently smooth natural surfaces, namely those with root mean square (rms) slope not larger than about 0.25, such as calm to moderate sea, asphalt, smooth terrain. In the case of very rough ground, the complementary GO-GO model in [22] might be adopted.

Final expressions of the bistatic scattered-field statistics are reported for a rough surface, possibly anisotropic, with a generic spectrum and specialized for normally and exponentially correlated surfaces.

Finally, to ensure reproducibility of results, the codes of the proposed model are publicly available at http://wpage.unina.it/alessio.disimone/download/download.htm (accessed on 13 April 2026).

The remaining part of the work is organized as follows: Section 2 introduces the theoretical framework adopted for scattering evaluation and the geometrical models of the composite scene; Section 3 presents the EM bistatic scattering model; numerical results and comparisons with the available literature are provided in Section 4 along with the validity limits of the proposed model; finally, concluding remarks are highlighted in Section 5.

2. Material and Methods

In this section, we introduce the theoretical background adopted to derive the bistatic scattering model. Remarkably, Section 2.1 briefly discusses the EM framework, namely the KA with its subsequent GO and PO solutions; Section 2.2 introduces the geometrical description of both the target and the surrounding rough surface.

2.1. Electromagnetic Scattering Framework

The scattering problem is solved under the assumption that the incident field is a plane wave, i.e.,

$$\underline{E}_{\mathrm{i}}(\underline{r}) = E_0 \hat{e}_{\mathrm{i}} \exp\left(jk\hat{k}_{\mathrm{i}} \cdot \underline{r}\right), \tag{1}$$

where $\underline{r}$ is the observation point, E_0 is the complex amplitude, $\hat{e}_{\mathrm{i}}$ denotes the polarization state of the incident field, $k = 2\pi/\lambda$ is the free-space EM wavenumber, λ being the corresponding wavelength, and $\hat{k}_{\mathrm{i}}$ is the propagation direction of the incident field. A periodic time dependence $\exp(-j\omega t)$ is understood and omitted.

In presence of a single, and possibly rough, scattering surface S delimiting two homogeneous media, the KA, and its subsequent GO and PO solutions, allow for the analytical evaluation of the field scattered in the upper medium, provided that the mean radius of curvature of the illuminated surface is much larger than the wavelength and that shadowing and multiple reflections do not take place over the scattering surface. In the case of a random rough surface, the validity conditions for KA can be expressed in terms of the surface roughness standard deviation and correlation length, as reported in Section 4.3 and also in ([8] ch. 12) and [22].

A polarimetric description of the scattering surface can be obtained by decomposing the incident and scattered fields into two mutually orthogonal polarization components named horizontal (subscript “h”) and vertical (subscript “v”). In this linear polarization basis, the scattered field can then be expressed as [9,20,24]

$$\begin{bmatrix} E_{\mathrm{sh}} \\ E_{\mathrm{sv}} \end{bmatrix} = jk\frac{e^{jkr}}{4\pi r} \iint_{\mathrm{A}_0} e^{j(\underline{k}_{\mathrm{i}} - \underline{k}_{\mathrm{s}})\cdot \underline{r}'} \cdot \underline{\underline{S}}(\hat{k}_{\mathrm{i}}, \hat{k}_{\mathrm{s}}, \hat{n}) \mathrm{d}x\mathrm{d}y \begin{bmatrix} E_{0\mathrm{h}} \\ E_{0\mathrm{v}} \end{bmatrix}, \tag{2}$$

where A_0 is the projection of the scattering surface S onto the mean plane xy; $\hat{k}_{\mathrm{s}}$ denotes the observation, or scattering, direction; $\hat{n}$ is the local normal to the surface S; and $E_{0\mathrm{h}}$ and $E_{0\mathrm{v}}$ are the complex amplitude of the horizontal and vertical components of the incident electric field $\underline{E}_{\mathrm{i}}$, respectively; similarly, E_{sh} and E_{sv} are the components of the scattered field.

In (2), $\underline{\underline{S}}(\hat{k}_{\mathrm{i}}, \hat{k}_{\mathrm{s}}, \hat{n})$ denotes the scattering matrix (also referred to as *scattering amplitude* or *polarization tensor*), that, under KA, still depends upon the local surface normal [20,22]. It is related to the slowly varying vector function $\underline{F}$ that depends upon the polarization, the slopes and the dielectric properties of the surface. Its full expression is reported in [20,22].

In the scattering reference frame reported in Figure 3, where the xy plane coincides with the rough surface mean plane, and the transmitter is located in the yz plane, the incident $\hat{k}_{\mathrm{i}}$ and scattered $\hat{k}_{\mathrm{s}}$ wave propagation directions can be written as

$$\hat{k}_\text{i} = -\sin\theta\hat{y} - \cos\theta\hat{z}\,, \tag{3}$$

$$\hat{k}_\text{s} = \sin\theta_\text{s}\cos\phi_\text{s}\hat{x} + \sin\theta_\text{s}\sin\phi_\text{s}\hat{y} + \cos\theta_\text{s}\hat{z}, \tag{4}$$

where $\theta \in [0, \pi/2]$ stands for the transmitter look angle, whereas $\theta_\text{s} \in [0, \pi/2]$ and $\phi_\text{s} \in [0, 2\pi]$ are the receiver polar and azimuth angles.

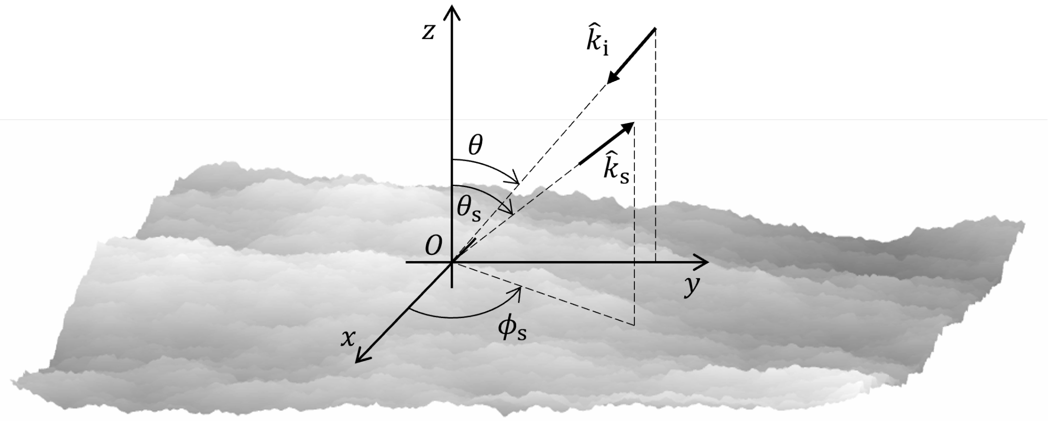

Figure 3. Reference system for the scattering problem. The transmitting source is located in the *yz* plane.

In this coordinate system, the entries S_{pq} of the scattering matrix can be expressed in terms of the Cartesian components of the vector functions $\underline{F}_\text{h}$ and $\underline{F}_\text{v}$, which stand for the vector function $\underline{F}$ evaluated for horizontally and vertically polarized incident field, respectively [22]:

$$S_\text{hh} = F_{\text{h}x}\sin\phi_\text{s} - F_{\text{h}y}\cos\phi_\text{s}\,, \tag{5a}$$
$$S_\text{vh} = F_{\text{v}x}\sin\phi_\text{s} - F_{\text{v}y}\cos\phi_\text{s}\,, \tag{5b}$$
$$S_\text{hv} = -F_{\text{h}x}\cos\theta_\text{s}\cos\phi_\text{s} - F_{\text{h}y}\cos\theta_\text{s}\sin\phi_\text{s} + F_{\text{h}z}\sin\theta_\text{s}\,, \tag{5c}$$
$$S_\text{vv} = -F_{\text{v}x}\cos\theta_\text{s}\cos\phi_\text{s} - F_{\text{v}y}\cos\theta_\text{s}\sin\phi_\text{s} + F_{\text{v}z}\sin\theta_\text{s}\,. \tag{5d}$$

We stress here that the above expressions of the cross-polarization scattering entries S_vh and S_hv were incorrectly reported by some of these authors in [22].

In presence of a random rough surface, the analytical evaluation of the scattered field in (2) requires the additional assumptions leading to the GO and PO solutions. A detailed description of such formulations goes beyond the scope of this work and is reported in [20,22]. Here it is recalled that under both PO and GO, the scattering matrix $\underline{\underline{S}}$ no longer changes over the scattering surface, and, consequently, the scattered field in (2) simplifies as follows:

$$\begin{bmatrix} E_\text{sh} \\ E_\text{sv} \end{bmatrix} = jk\frac{e^{jkr}}{4\pi r}\underline{\underline{S}}\begin{bmatrix} E_\text{0h} \\ E_\text{0v} \end{bmatrix} I_{\text{A}_0}\,, \tag{6}$$

where

$$I_{\text{A}_0} = \iint_{\text{A}_0} e^{jk(\eta_x x + \eta_y y + \eta_z z(x,y))}\text{d}x\text{d}y \tag{7}$$

is the scattering integral, that accounts only for the surface roughness through the height profile $z(x,y)$; $\underline{\eta} = \hat{k}_\text{i} - \hat{k}_\text{s}$. It is also recalled that, under GO, the scattering matrix does no longer depend upon the surface local normal due to the specular reflection condition:

$$\hat{k}_\text{s} = \hat{k}_\text{i} - 2(\hat{k}_\text{i}\cdot\hat{n})\hat{n}. \tag{8}$$

https://doi.org/10.3390/rs18081219

From (6) and (7) it is evident that, in presence of a random rough scattering surface, the coherent and incoherent components of the scattered field can be obtained once the entries of the scattering matrix in (5d) and the mean $\langle I_{A_0} \rangle$ and variance $\sigma^2_{A_0}$ of the scattering integral in (7) are evaluated. It is also worth recalling that, under PO, the latter depends on the surface spectrum through the nth-order power spectrum [8,9], which is discussed in the next Section 2.2.

Finally, a last remark on the validity limits. The GO solution is valid if KA holds, and if, additionally, the kernel of the integral in (2) is rapidly oscillating, which requires $(k\eta_z\sigma)^2 > 10$ ([8] ch. 12). Conversely, the zeroth-order PO solution holds in the small local slopes regime, i.e., if the rms of the surface local slopes is lower than 0.25 ([8] ch. 12). Additionally, the modulus of $k\sigma\eta_z$ has to be sufficiently small in order to ensure power series convergence of the scattering integral kernel in the evaluation of the field variance. It is then evident that GO and PO provide somehow complementary validity limits. However, a deeper discussion on the validity limits of the proposed scattering model is reported in Section 4.3.

2.2. Geometrical Models

The geometry of the scattering problem is shown in Figure 4, where an electromagnetically large target lies over a lossy rough background surface with complex permittivity $\varepsilon_{\mathrm{r}}^{\mathrm{G}}$. The target is modeled as a dielectric parallelepiped with complex permittivity $\varepsilon_{\mathrm{r}}^{\mathrm{W}}$ and smooth walls of length l_m, $m = 1,2,3,4$, and height h (it is assumed then that $l_1 = l_3$ and $l_2 = l_4$). The vertical faces of the target are parallel to the z-axis and, then, the unit vector normal to such faces is

$$\hat{n}_{\mathrm{W}_m} = \sin\phi_m \hat{x} + \cos\phi_m \hat{y}, \quad m = 1,2,3,4\,, \tag{9}$$

where $\phi_m = \phi_1 + (m-1)\pi/2$ is the angle between the positive x-semiaxis and the base of the wall of length l_m, measured clockwise. Additionally, we assume that the center of the target roof, i.e., the top horizontal face, is located at $(\bar{x}_0, \bar{y}_0, h)$, so that the center of the mth target wall base is located at $(x_m, y_m, 0)$ with, see Figure 4,

$$x_m = \bar{x}_0 + \frac{l_{m\pm1}}{2}\sin\phi_m, \tag{10a}$$

$$y_m = \bar{y}_0 + \frac{l_{m\pm1}}{2}\cos\phi_m. \tag{10b}$$

The rough background is modeled as a finite-size 2-D zero-mean normally distributed random process with height variance σ^2, normalized ACF $\rho(\tau_x, \tau_y)$, where τ_x and τ_y are the distances along the x- and y-axes between the two generic surface points. Results are reported for a generic ACF, possibly anisotropic, while closed-form expressions of the scattered-field statistics can easily be obtained for normally or exponentially correlated rough surfaces, either isotropic or anisotropic.

The nth-order roughness power spectrum (normalized to σ^{2n}) is defined here as follows [25,26]

$$W^{(n)}(k_x, k_y) = \iint_{-\infty}^{+\infty} \rho^n(\tau_x, \tau_y) e^{jk_x\tau_x + jk_y\tau_y}\, d\tau_x\, d\tau_y \tag{11}$$

where k_x and k_y are the spatial frequency counterparts of the spatial variables τ_x and τ_y, respectively.

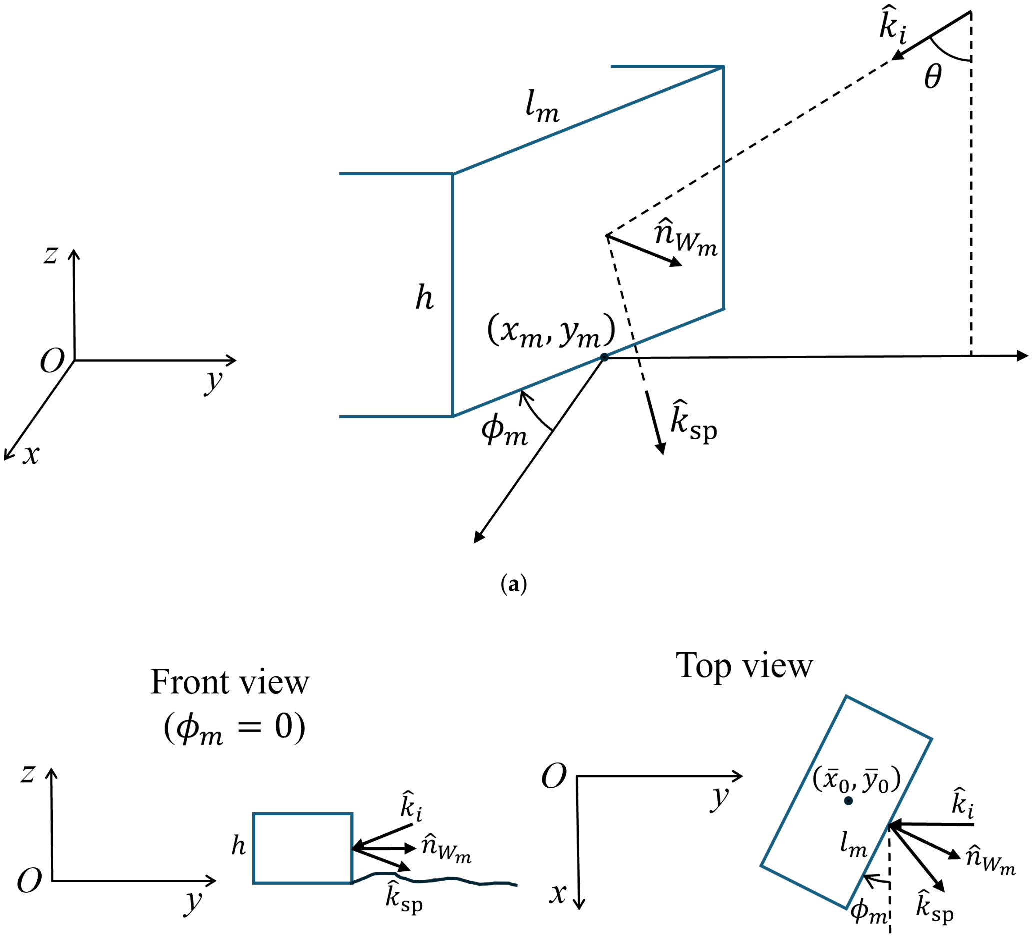

(**a**)

(**b**) (**c**)

Figure 4. Geometry of the scattering problem with illustration of the target wall reflection. (**a**) 3-D view; (**b**) front view for $\phi_m = 0$; (**c**) top view.

The roughness power spectrum of order n can be expressed in closed form for the above-mentioned rough surface types, see Table 1, where $\tau = \sqrt{\tau_x^2 + \tau_y^2}$ is the distance between two generic surface points, l_c stands for the isotropic surface correlation length, and, finally, l_x and l_y stand for the correlation lengths of the anisotropic surface along the x- and y-axis, respectively. It is worth noting that other correlation functions, such as the "mixed" and the "intermediate" functions defined in [27] do not lead to closed forms of the nth-order power spectrum. In the case that no analytical expression exists for the nth-order roughness power spectrum, a two-fold numerical integration is required to evaluate (11) and, then, the scattered field. Finally, in the case the nth-order surface power spectrum is assigned, (11) can be reverted either analytically or numerically to get the normalized ACF as follows:

$$\rho(\tau_x, \tau_y) = \left[\frac{1}{4\pi^2} \iint\limits_{-\infty}^{+\infty} W^{(n)}(k_x, k_y) e^{-jk_x\tau_x - jk_y\tau_y} \, dk_x \, dk_y \right]^{1/n}. \tag{12}$$

This could be of interest for, e.g., sea surface, whose second-order statistics are typically assigned through the power spectrum, i.e., in our notation $\sigma^2 W^{(1)}(k_x, k_y)$. Conversely, bare soil surfaces are typically described via the ACF.

In the case of the normally distributed isotropic random rough surface, the rms local slope is $\sigma_s = \sigma(|\rho''(0)|)^{1/2}$, where $\rho''(\cdot)$ is the second derivative of the ACF. For anisotropic normally distributed surfaces, the rms local slopes along x and y can be evaluated as $\sigma_{s,x} = \sigma(|\rho_{\tau_x\tau_x}(0,0)|)^{1/2}$ and $\sigma_{s,y} = \sigma(|\rho_{\tau_y\tau_y}(0,0)|)^{1/2}$, respectively, where $\rho_{\tau_x\tau_x}(\cdot,\cdot)$ and

$\rho_{\tau_y\tau_y}(\cdot,\cdot)$ are the second-order partial derivatives of the anisotropic ACF $\rho(\tau_x,\tau_y)$ with respect to τ_x and τ_y, respectively. Finally, the overall local rms slope can be evaluated as $\sigma_s = \sqrt{\sigma_{s,x}^2 + \sigma_{s,y}^2}$.

Table 1. *N*th-order power spectrum for normally and exponentially correlated random rough surfaces.

Surface Type	Normalized ACF	*n*th-Order PSD
Gaussian isotropic	$\rho(\tau) = \exp\left(-\frac{\tau^2}{l_c^2}\right)$	$W^{(n)}(k_x,k_y) = \frac{\pi}{n} l_c^2 \exp\left[-\frac{l_c^2}{4n}(k_x^2+k_y^2)\right]$
Gaussian anisotropic	$\rho(\tau_x,\tau_y) = \exp\left(-\frac{\tau_x^2}{l_x^2} - \frac{\tau_y^2}{l_y^2}\right)$	$W^{(n)}(k_x,k_y) = \frac{\pi}{n} l_x l_y \exp\left[-\frac{k_x^2 l_x^2 + k_y^2 l_y^2}{4n}\right]$
Exponential isotropic	$\rho(\tau) = \exp\left(-\frac{\tau}{l_c}\right)$	$W^{(n)}(k_x,k_y) = 2\pi \frac{n}{l_c}\left[k_x^2 + k_y^2 + \left(\frac{n}{l_c}\right)^2\right]^{-\frac{3}{2}}$
Exponential anisotropic	$\rho(\tau_x,\tau_y) = \exp\left(-\sqrt{\frac{\tau_x^2}{l_x^2} + \frac{\tau_y^2}{l_y^2}}\right)$	$W^{(n)}(k_x,k_y) = 2\pi n l_x l_y \left(k_x^2 l_x^2 + k_y^2 l_y^2 + n^2\right)^{-\frac{3}{2}}$

Finally, a last remark about sea surface modeling. Actually, the proposed scattering formulation starts from the fundamental assumption of Gaussian height distribution for the rough surface height. This hypothesis allows keeping the full mathematical tractability of the considered scattering problem and is a common assumption in microwave scattering from random rough surfaces, including sea surface (as reported in the classical textbooks on the topic). Within the context of ocean scatterometry, this model is also referred to as linear sea surface model, which assumes that each surface harmonic propagates according to the dispersion relation typical of water waves [28]. However, the non-linear hydrodynamics coupling the motion of the large and small waves may change the statistical characteristics of the surface wave components, such as mean, rms slope and spectrum, and then impact on microwave scattering from sea surface. Indeed, non-linear sea surface models typically exhibit non-zero-mean and non-Gaussian height distribution with slightly increased rms slope w.r.t. the linear model [28]. As a result, the proposed model does not explicitly account for such non linearities with potential underestimation of the scattered field. A possible approach for implementing the non-linear sea model within the proposed formulation could exploit the Choppy Wave Model (CWM) discussed in [29] as outlined in [28] for the SSA-2 model. Notwithstanding, the expected magnification of the rms slopes induced by the non-linear CWM transformation of the sea surface may generate small errors in the estimation of the RCS, as detailed in [28]. Additionally, advanced sea spectrums (e.g., Elfouhaily, Pierson–Moscowitz, Apel) based on measurements inherently account for non-linear features and, therefore, the induced errors might be partially compensated if such measurements-based sea spectrum models are adopted in the proposed framework. To this end, we stress here that the proposed GO-PO model is able to deal with any arbitrary surface spectrum, given that the surface roughness is normally distributed. Indeed, as discussed above, under this assumption, the rough surface ACF can be derived from the assigned roughness spectrum through (12) and, then, the roughness power spectrum of order n can be evaluated via (11). Accordingly, it can be reasonably expected that the inclusion of such higher-order effects could lead to limited improvements of accuracy compared to other simplifying hypotheses of the proposed scattering model, such as the adoption of the zeroth-order PO solution and the simplified target geometry. Notwithstanding, from a model perspective, in the case of non-Gaussian surfaces, such as non-linear sea surface, the derivation of the PO solution should be adapted to accommodate the surface roughness characteristic function appearing in the scattering integral evaluation.

3. GO-PO Bistatic Scattering Model

By following the approaches reported in [20,22], in this section we provide analytical expressions of the EM field scattered from the scene shown in Figure 2. According to Section 2.1, the scattered field is a random process due to the randomness of the background surface and, hence, we focus on the evaluation of the mean and variance of the field. Remarkably, for each of the scattering contributions shown in Figure 2, we provide expressions of the scattering matrix entries S_{pq} and the mean $\langle I_{A_0} \rangle$ and variance $\sigma^2_{A_0}$ of the scattering integral I_{A_0}. The Fresnel reflection coefficients for the wall and ground will be denoted hereafter with the "W" and "G" superscripts, respectively.

As already stated in Section 1, here we use the GO solution to describe scattering from the target walls, with the exception of the single-reflection terms for which KA can be adopted without any further approximation, as detailed later in this section. Conversely, scattering from ground is modeled via PO, at variance of [22] where ground scattering is described via GO. Accordingly, we refer to this model as the GO-PO bistatic scattering model. Indeed, as the target walls are smooth and much larger compared to the operating wavelength, the field scattered from them can be well approximated in the framework of GO as plane waves reflected in the specular reflection direction, that depends on the direction of the impinging field and the orientation of the target, see (8). In other words, the target walls act as an EM mirror specularly reflecting the impinging energy. The only exception is the single-scattering contribution from the wall, as, in this case, under GO, the field scattered from the wall would be zero but in the limiting case of $\theta \rightarrow \pi/2$ [20]. As a matter of fact, this scattering contribution can be evaluated analytically under KA, without any further approximation.

Additionally, to complement the analysis in [22], here we assume that the background surface is gently to moderately rough, so that the PO solution can be applied to reflections from the ground. As it will be demonstrated in this section, the PO solution can describe the anisotropic roughness through the 2-D surface roughness spectrum of order n, $W^{(n)}$, introduced in Section 2.2 and evaluated in Table 1 for different ACF types. Indeed, the surface spectrum function is one of the parameters ruling the target-ground coupling and, then, directly impacts on the target bistatic RCS via the multiple-reflection terms analyzed in Sections 3.2 and 3.3.

A brief justification for the selected scattering solutions is now in order. The choice of the scattering models for describing the EM behavior of the rough ground surface and the target has been carried out based on both their main geometrical features and the requirement of keeping the mathematical treatability of the scattering problem. As a preliminary consideration, we also underline that, as already briefly discussed in Section 2.1, both GO and PO derive from the KA, which acts as a common framework for our scattering model.

The considered targets (e.g., large buildings and ships) exhibit negligible roughness and large electrical sizes at microwaves and, accordingly, the scattering from such structures can be adequately described in the framework of the high-frequency ray-optics limit, i.e., GO. En passant, we stress here that the adoption of the GO model also enables the derivation of closed-form expressions for the multiple-bounce terms and, hence, the analytical evaluation of the EM coupling effects between the ground and the target. Indeed, according to GO, the wave scattered from the target walls can be well approximated by a plane wave propagating in a specific direction depending upon the incident field direction and target orientation, and whose amplitude is described by means of the scattering matrix.

As for the rough ground surface, in this work we focus on such surfaces exhibiting sufficiently small local slopes (rms slope not larger than 0.25), such as sea with no breaking waves, asphalt, smooth terrain. In this hypothesis, PO is a good candidate for describing the ground surface scattering.

The same methodology based on the selection of different models for scattering from the target and the ground has been already investigated in different works, see, e.g., [20–22]. Indeed, multiple reflections can be rigorously described provided that the selected models for scattering from the target and the ground can be formulated in a common theoretical background, so that it is possible to define unambiguously a proper scattering matrix and scattering integral. In our GO-PO model, the common framework is the KA, where all the scattering contributions can be expressed according to (6) and (7). Remarkably, by following an approach similar to those in [20–22], the scattering matrix relevant to the multiple reflection terms can be expressed as the multiplication of a proper set of elementary scattering matrices relevant to the reflections upon the target wall and the ground, whereas for the scattering integral evaluation, a proper scattering area and kernel have to be defined depending on the reflection term and the scattering geometry.

It is worth mentioning that, for the sake of brevity, here we provide expressions of only S_{hh} and S_{vh} as the remaining entries of the scattering matrix, namely S_{vv} and S_{hv}, relevant to the generic N-bounce contribution can easily be recovered from the following relations ([24] Appendix)

$$S_{\mathrm{vv}}\left(\underline{R}_{\perp},\underline{R}_{//}\right)=S_{\mathrm{hh}}\left(\underline{R}_{//},\underline{R}_{\perp}\right) \tag{13a}$$

$$S_{\mathrm{hv}}\left(\underline{R}_{\perp},\underline{R}_{//}\right)=-S_{\mathrm{vh}}\left(\underline{R}_{//},\underline{R}_{\perp}\right) \tag{13b}$$

where $\underline{R}_{\perp}=[R_{\perp,1},R_{\perp,2},...,R_{\perp,N}]$ and $\underline{R}_{//}=[R_{//,1},R_{//,2},...,R_{//,N}]$ are the N-tuples of Fresnel reflection coefficients, with $R_{\perp,i}$ and $R_{//,i}$ for $i=1,2,...,N$ being the Fresnel coefficients of the ith bounce (either from ground or wall), for locally perpendicular and parallel polarizations, respectively. Conditions (13a) and (13b) reveal that we can move from S_{hh} to S_{vv}, or viceversa, by simply exchanging any $R_{\perp}$ with the corresponding $R_{//}$ and viceversa. The same applies for the cross-pol entries S_{vh} and S_{hv} with an additional overall sign change.

Finally, in this section, expressions of the variance $\sigma^2_{A_0}$ of the scattering integral are provided for a generic rough surface, possibly anisotropic, with nth-order roughness power spectrum $W^{(n)}(\cdot,\cdot)$. However, an analytical formulation of the mean and variance of the field scattered from a rough surface with Gaussian or exponential ACF can easily be derived by replacing the nth-order power spectrum with the proper expression from Table 1.

Starting from the coherent and incoherent components of each scattering contribution, the overall scattered field and RCS are evaluated as detailed in [20,22]. Remarkably, the overall random scattered field $\underline{E}_{\mathrm{s}}$ can be expressed as the superposition of the field scattered from ground surface $\underline{E}_{\mathrm{s,ground}}$ and the target $\underline{E}_{\mathrm{s,target}}$, i.e.,

$$\underline{E}_{\mathrm{s}}=\underline{E}_{\mathrm{s,ground}}+\underline{E}_{\mathrm{s,target}} \tag{14}$$

where $\underline{E}_{\mathrm{s,target}}$ can in turn be decomposed as follows:

$$\underline{E}_{\mathrm{s,target}}=\underline{E}_{\mathrm{s,roof}}+\sum_{m=1}^{4}\left(\underline{E}_{\mathrm{s,W},m}+\underline{E}_{\mathrm{s,WG},m}+\underline{E}_{\mathrm{s,GW},m}+\underline{E}_{\mathrm{s,WGW},m}\right) \tag{15}$$

where $\underline{E}_{\mathrm{s,roof}}$ and $\underline{E}_{\mathrm{s,W},m}$ are the single-bounce fields scattered from the target roof, i.e., the top horizontal face of the parallelepiped, and the mth target wall, i.e., the mth vertical face, respectively (green lines in Figure 2); $\underline{E}_{\mathrm{s,WG},m}$ and $\underline{E}_{\mathrm{s,GW},m}$ are the double-bounce scattering terms (blue lines in Figure 2) arising from the interaction between the ground surface and the mth target wall; finally, $\underline{E}_{\mathrm{s,WGW},m}$ is the mth wall triple-bounce term (yellow line in Figure 2). It is worth mentioning that the multiple-bounce terms in (15) account for the EM coupling between the target and the surrounding ground. Each scattering term appearing in (14) and (15) can be expressed as in (6), with proper scattering matrix and scattering integral. While the former is deterministic in the considered scattering problem, the latter is deterministic only for the single-bounce terms from the target roof and walls, being random for all other terms which involve a reflection off the rough ground.

The mean square value of the q-polarized component of the overall scattered field can be written as

$$\langle |E_{sq}|^2 \rangle = |\langle E_{sq} \rangle|^2 + \mathrm{VAR}(E_{sq}) \tag{16}$$

where $\langle E_{sq} \rangle$ and $\mathrm{VAR}(E_{sq})$ are the coherent and incoherent components of the scattered field $\langle \cdot \rangle$ and $\mathrm{VAR}(\cdot)$ standing for the statistical mean and variance, respectively. The mean value $\langle E_{sq} \rangle$ can be easily recast as the sum of the coherent components from the ground and the target, i.e.,

$$\langle E_{sq} \rangle = \langle E_{sq,\mathrm{ground}} \rangle + \langle E_{sq,\mathrm{target}} \rangle \tag{17}$$

where

$$\langle E_{sq,\mathrm{target}} \rangle = E_{sq,\mathrm{roof}} + \sum_{m=1}^{4} \big(E_{sq,\mathrm{W},m} + \langle E_{sq,\mathrm{WG},m} \rangle + \langle E_{sq,\mathrm{GW},m} \rangle + \langle E_{sq,\mathrm{WGW},m} \rangle \big), \tag{18}$$

the single-bounce terms from the target roof and walls being deterministic in the considered target geometry. The overall field variance can be decomposed as follows

$$\mathrm{VAR}(E_{sq}) = \mathrm{VAR}(E_{sq,\mathrm{ground}}) + \mathrm{VAR}(E_{sq,\mathrm{target}}) \tag{19}$$

where

$$\begin{aligned} \mathrm{VAR}(E_{sq,\mathrm{target}}) = \sum_{m=1}^{4} \big[& \mathrm{VAR}(E_{sq,\mathrm{WG},m}) + \mathrm{VAR}(E_{sq,\mathrm{GW},m}) \\ & + \mathrm{VAR}(E_{sq,\mathrm{WGW},m}) + 2\,\mathrm{Re}(\mathrm{COV}(E_{sq,\mathrm{WG},m}, E_{sq,\mathrm{GW},m})) \big] \end{aligned} \tag{20}$$

where $\mathrm{Re}(\cdot)$ and COV denote the real part and the covariance operators, respectively. In (19) and (20) we make the assumption of uncorrelation among those scattering terms undergoing different reflection mechanisms as motivated in [20]. Such a hypothesis does not apply to the double-bounce terms as in specific configurations they are strongly correlated. This point, that is more deeply investigated in this section, can easily be motivated by the fact that such contributions coincide in the backscattering case, as it is the case in [20], where the two double-bounce terms are indeed treated jointly. These considerations motivate the covariance term in (20).

Finally, the RCS of either the ground or the target in the pq polarization channel can be evaluated from the mean square value of the corresponding scattered field as follows [20]

$$\mathrm{RCS}_{pq} = 4\pi r^2 \frac{\langle |E_{sq}|^2 \rangle}{|E_{0p}|^2}. \tag{21}$$

The composite RCS is obtained by considering in (21) the total scattered field in (14).

3.1. Single-Bounce Contributions

In this section, we provide expressions for the contributions to the overall scattered field related to the single reflections from either the ground or the target walls and rooftop (see the green lines in Figure 2). Such contributions are well studied in the classical theory of EM scattering from rough surfaces, see, e.g., [7–9,20].

The single bounce from the rough ground can be evaluated by directly applying (5d) and (6) with $\hat{n} = \hat{z}$. The scattering matrix as well as the mean and variance of the scattering integral I_{A_0} are provided in Table 2 for a generic surface with nth-order roughness power spectrum $W^{(n)}(\cdot,\cdot)$ and with dimensions a and b along y and x, respectively. In Table 2, $R_{\perp}^{\mathrm{G}}(\theta)$ and $R_{//}^{\mathrm{G}}(\theta)$ are the perpendicular and parallel Fresnel reflection coefficients relevant to the ground. Therefore, $R_{\perp}^{\mathrm{G}}(\theta) = R_{\perp}(\varepsilon_{\mathrm{r}}^{\mathrm{G}}, \theta)$ and $R_{//}^{\mathrm{G}}(\theta) = R_{//}(\varepsilon_{\mathrm{r}}^{\mathrm{G}}, \theta)$.

As specific cases, the variance of the scattering integral $\sigma_{A_0}^2$ can be expressed in closed form as follows

$$\sigma_{A_0}^2 = \exp\left(-k^2\sigma^2\eta_z^2\right) ab\pi l_c^2 \sum_{n=1}^{+\infty} \frac{(k\sigma\eta_z)^{2n}}{n!n} \exp\left[-\frac{k^2 l_c^2}{4n}\left(\eta_x^2+\eta_y^2\right)\right] \tag{22}$$

in the presence of an isotropic rough surface with Gaussian ACF, or as

$$\sigma_{A_0}^2 = \exp\left(-k^2\sigma^2\eta_z^2\right) ab\frac{2\pi}{l_c} \sum_{n=1}^{+\infty} \frac{(k\sigma\eta_z)^{2n}}{(n-1)!} \left[k^2(\eta_x^2+\eta_y^2) + \left(\frac{n}{l_c}\right)^2\right]^{-\frac{3}{2}} \tag{23}$$

if the rough surface is exponentially correlated. In (22) and (23), the vector difference $\underline{\eta} = \eta_x\hat{x} + \eta_y\hat{y} + \eta_z\hat{z}$ is reported in Table 2.

Table 2. Single-scattering contribution from ground.

$$S_{\mathrm{hh}} = \sin\phi_{\mathrm{s}}\left[R_{\perp}^{\mathrm{G}}(\theta)(\cos\theta + \cos\theta_{\mathrm{s}}) + \cos\theta_{\mathrm{s}} - \cos\theta\right]$$

$$S_{\mathrm{vh}} = \cos\phi_{\mathrm{s}}\left[R_{//}^{\mathrm{G}}(\theta)(1 + \cos\theta\cos\theta_{\mathrm{s}}) + 1 - \cos\theta\cos\theta_{\mathrm{s}}\right]$$

$$\begin{aligned}\langle I_{\mathrm{A}_0}\rangle &= ab\,\exp\left(-\frac{k^2\sigma^2\eta_z^2}{2}\right)\mathrm{sinc}\left(\frac{ka\eta_y}{2}\right)\mathrm{sinc}\left(\frac{kb\eta_x}{2}\right)\\ \sigma_{A_0}^2 &= \langle|I_{\mathrm{A}_0}|^2\rangle - |\langle I_{A_0}\rangle|^2\\ &= \exp(-k^2\sigma^2\eta_z^2)ab\sum_{n=1}^{+\infty}\frac{(k\sigma\eta_z)^{2n}}{n!}W^{(n)}(k\eta_x, k\eta_y)\end{aligned}$$

$$\begin{aligned}\eta_x &= -\sin\theta_s\cos\phi_s\\ \eta_y &= -\sin\theta - \sin\theta_s\sin\phi_s\\ \eta_z &= -\cos\theta - \cos\theta_s\end{aligned}$$

It might be worth noting that all the entries of the scattering matrix still depend upon ϕ_s also in the limiting case of $\theta_s = 0$, i.e., with the receiver located along the z-axis. Even though this might seem unexpected, we should recall here that the actual intensity of the scattered field is proportional to $|S_{pp}|^2 + |S_{pq}|^2$, i.e., both co- and cross-polarized components of the scattered field must be considered. For example, an horizontally transmitted field is associated with a scattered field whose intensity is related to $|S_{\mathrm{hh}}|^2 + |S_{\mathrm{hv}}|^2$, that can be expressed as

$$\begin{aligned}|S_{\mathrm{hh}}|^2 + |S_{\mathrm{hv}}|^2 = &+ |R_{\perp}^{G}|^2\left[(\cos\theta + \cos\theta_s)^2 + \cos^2\phi_s\left(1-\cos^2\theta\right)\left(1-\cos^2\theta_s\right)\right]\\ &+ 2R_{\perp}^{G}\left[\cos^2\theta_s - \cos^2\theta + \cos^2\phi_s\left(1-\cos^2\theta_s\right)\left(1+\cos^2\theta\right)\right]\\ &+ (\cos\theta - \cos\theta_s)^2 + \cos^2\phi_s\left(1-\cos^2\theta\right)\left(1-\cos^2\theta_s\right)\end{aligned} \tag{24}$$

It can be noted that (24) no longer depends upon ϕ_s in the case that $\theta_s = 0$, as it could be physically expected, the dependence of the single polarization components being instead related to the mathematical dependence of the polarization state unit vectors $\hat{e}_{\mathrm{sh}}$ and $\hat{e}_{\mathrm{sv}}$ upon ϕ_s [22].

Let us move to the single-scattering terms from the target. The single-scattering contribution from the target roof is a deterministic term that, under KA, can easily be evaluated from (2) without any further approximation. The scattering integral I_{A_0} for such a term reads as

$$\begin{aligned} I_{A_0} =& \exp(jk\eta_x\overline{x}_0)\exp(jk\eta_y\overline{y}_0)\exp(jk\eta_z h)l_1 l_2 \\ &\times \operatorname{sinc}\left[\frac{kl_1}{2}(\eta_x\cos\phi_1-\eta_y\sin\phi_1)\right] \\ &\times \operatorname{sinc}\left[\frac{kl_2}{2}(\eta_x\sin\phi_1+\eta_y\cos\phi_1)\right] \end{aligned} \tag{25}$$

where $\operatorname{sinc}(x) = \sin(x)/x$, $\eta_x = -\sin\theta_s\cos\phi_s$, $\eta_y = -\sin\theta - \sin\theta_s\sin\phi_s$, $\eta_z = -\cos\theta - \cos\theta_s$, and h stands for the target height. In addition, it can easily be shown by inspection of ([20] Equation (3.13)) that the scattering matrix relevant to such a scattering term formally coincides with that related to the single scattering from ground (see Table 2) as long as the dielectric constant of the ground is properly replaced with that of the target.

Similarly to the scattering from the target rooftop, the scattering integrals relevant to the contributions from the walls can be evaluated analytically and are no longer random. Indeed, for such a contribution no expansion of the vector function $\underline{F}$ is necessary, and, therefore, PO coincides with KA. Table 3 reports the results for the single-scattering from the wall, hence evaluated according to KA. In this case, the local incidence angle on the mth wall, called ψ_m, depends upon both the transmitter look angle θ and the orientation angle of the wall ϕ_m. Indeed, it can be evaluated as

$$\psi_m = \cos^{-1}\left(-\hat{k}_\mathrm{i}\cdot\hat{n}_{\mathrm{W}_m}\right) \tag{26}$$

and its expression is reported in Table 3, where $R_\perp^\mathrm{W}(\psi_m)$ and $R_{//}^\mathrm{W}(\psi_m)$ are the perpendicular and parallel Fresnel reflection coefficients relevant to the wall. Therefore, $R_\perp^\mathrm{W}(\psi_m) = R_\perp(\varepsilon_\mathrm{r}^\mathrm{W},\psi_m)$ and $R_{//}^\mathrm{W}(\psi_m) = R_{//}(\varepsilon_\mathrm{r}^\mathrm{W},\psi_m)$.

Table 3. Single-scattering contribution from wall (KA).

$$\begin{aligned} S_\mathrm{hh} =& -1/\sin^2\psi_m\Big\{-R_\perp^\mathrm{W}(\psi_m)\sin^2\psi_m\left[-\sin\theta_\mathrm{s}\cos\phi_m+\sin\theta\sin(\phi_m+\phi_\mathrm{s})\right]\left[\cos^2\theta\sin\theta_\mathrm{s}\cos\phi_m+\cos^2\theta\sin\theta\cos^2\phi_m\sin(\phi_m+\phi_\mathrm{s})\right. \\ &\left.+\cos\theta\sin\theta\cos\theta_\mathrm{s}\cos\phi_m\sin\phi_m\cos(\phi_m+\phi_\mathrm{s})\right]+R_{//}^\mathrm{W}(\psi_m)\left[\sin\theta\sin^2\phi_m\sin(\phi_m+\phi_\mathrm{s})+\sin^2\theta\sin\theta_\mathrm{s}\cos\phi_m\sin^2\phi_m\right. \\ &\left.-\cos\theta\sin\theta\cos\theta_\mathrm{s}\cos\phi_m\sin\phi_m\cos(\phi_m+\phi_\mathrm{s})\right]\Big\}, \end{aligned}$$

$$\begin{aligned} S_\mathrm{vh} =& -1/\sin^2\psi_m\Big\{+R_\perp^\mathrm{W}(\psi_m)\sin^2\psi_m\left[\sin\theta_\mathrm{s}\cos\theta\sin\phi_m+\sin\theta\cos\theta_\mathrm{s}\cos(\phi_m+\phi_\mathrm{s})\right]\left[\cos\theta\sin\theta_\mathrm{s}\sin\phi_m+\sin\theta\cos\theta_\mathrm{s}\sin^2\phi_m\cos(\phi_m+\phi_\mathrm{s})\right. \\ &\left.+\sin\theta\cos\theta\sin\phi_m\cos\phi_m\sin(\phi_m+\phi_\mathrm{s})\right]+R_{//}^\mathrm{W}(\psi_m)\left[\sin\theta\cos\theta\sin\phi_m\cos\phi_m\sin(\phi_m+\phi_\mathrm{s})+\sin^2\theta\cos\theta\sin\theta_\mathrm{s}\sin\phi_m\cos^2\phi_m\right. \\ &\left.-\sin\theta\cos^2\theta\cos\theta_\mathrm{s}\cos^2\phi_m\cos(\phi_m+\phi_\mathrm{s})\right]\Big\}, \end{aligned}$$

$$\psi_m = \cos^{-1}(\sin\theta\cos\phi_m)$$

$$I_{A_0} = l_m h\cos\phi_m\exp(jkx_m\eta_x)\exp(jky_m\eta_y)\exp\left(\frac{jkh\eta_z}{2}\right)\operatorname{sinc}\left(\frac{kl_m}{2}(\eta_x\cos\phi_m-\eta_y\sin\phi_m)\right)\operatorname{sinc}\left(\frac{kh\eta_z}{2}\right)$$

$$\begin{aligned} \eta_x &= -\sin\theta_s\cos\phi_s \\ \eta_y &= -\sin\theta-\sin\theta_s\sin\phi_s \\ \eta_z &= -\cos\theta-\cos\theta_s \end{aligned}$$

It is worth noting that the single-scattering term from the wall exists only if the wall is directly illuminated by the transmitter, which happens if

$$\hat{n}_{\mathrm{W}_m}\cdot\left(-\hat{k}_\mathrm{i}\right) > 0\,, \tag{27}$$

that can be recast as $\cos\phi_m > 0$.

3.2. Double-Bounce Contributions

The double-bounce terms of the overall scattered field refer to such contributions undergoing a double reflection, namely wall–ground (WG) and ground–wall (GW), see the solid and dashed blue lines in Figure 2, respectively. As already discussed in Section 3, such contributions coincide in the backscattering case, as long as scattering from the wall is modeled via GO [20]. However, they are no longer equal in a generic bistatic geometry as the propagation paths in the WG contribution (transmitter–wall–ground–receiver) and in the GW one (transmitter–ground–wall–receiver) differ in terms of overall length and local incidence angles on the wall. The latter, denoted here as ψ_m and $\overline{\psi}_m$, are the same as in the GO-GO model [22], while the local incidence angles on the ground differ from those derived in [22] due to the different surface normal unit vectors involved in scattering under GO and PO, namely $\hat{n}_{\mathrm{s}}$ and $\hat{n}_0$.

As for the WG terms, a plane wave propagating in the direction $\hat{k}_{\mathrm{sp}}$ emerges after reflection off the wall, see Figure 4, where [20,22]

$$\hat{k}_{\mathrm{sp}} = \sin\theta\sin 2\phi_m\hat{x} + \sin\theta\cos 2\phi_m\hat{y} - \cos\theta\hat{z}\,. \tag{28}$$

Accordingly, the overall scattering matrix $\underline{\underline{S}}^{\mathrm{WG}}$ relevant to the WG contribution can be evaluated as follows

$$\underline{\underline{S}}^{\mathrm{WG}} = \underline{\underline{S}}^{\mathrm{G}}(\hat{k}_{\mathrm{sp}}, \hat{k}_s, \hat{z})\underline{\underline{S}}^{\mathrm{W}}(\hat{k}_{\mathrm{i}}, \hat{k}_{\mathrm{sp}})\,, \tag{29}$$

where $\underline{\underline{S}}^{\mathrm{G}}$ and $\underline{\underline{S}}^{\mathrm{W}}$ refer to the scattering matrices relevant to the reflection off the ground and wall, respectively, evaluated according to ([20] Equation (3.13)) with the proper input unit wavevectors and surface normal.

The target walls contributing to the WG term are those directly illuminated by the transmitter, i.e., those for which (27) applies, i.e., $\cos\phi_m > 0$. However, the scattering area A_0' actually contributing to the WG scattered field depends also on the receiver position and different expressions of A_0' can be derived depending on the target orientation and acquisition geometry, see Table 4. Remarkably, if $\hat{k}_{\mathrm{s}} \cdot \hat{n}_{\mathrm{W}_m} < 0$, i.e., $\sin(\phi_s + \phi_m) < 0$, the scattering area might be partially or totally shadowed.

As for the GW terms (see Figure 5), the plane wave reaching the receiver after the double reflection is the one that is specularly reflected from the wall in the observation direction $\hat{k}_{\mathrm{s}}$, i.e., the one propagating in the direction $\hat{k}_{\mathrm{sg}}$ after reflection off the rough surface, where [22]

$$\hat{k}_{\mathrm{sg}} = \sin\theta_{\mathrm{s}}\cos(\phi_{\mathrm{s}} + 2\phi_m)\hat{x} - \sin\theta_{\mathrm{s}}\sin(\phi_{\mathrm{s}} + 2\phi_m)\hat{y} + \cos\theta_{\mathrm{s}}\hat{z}\,. \tag{30}$$

is evaluated according to the specular reflection condition in (8).

The scattering matrix $\underline{\underline{S}}^{\mathrm{GW}}$ relevant to the GW contribution can be evaluated as

$$\underline{\underline{S}}^{\mathrm{GW}} = \underline{\underline{S}}^{\mathrm{W}}(\hat{k}_{\mathrm{sg}}, \hat{k}_s)\underline{\underline{S}}^{\mathrm{G}}(\hat{k}_{\mathrm{i}}, \hat{k}_{\mathrm{sg}}, \hat{z})\,, \tag{31}$$

As opposed to the WG terms, GW contributions might also arise from target walls not directly illuminated by the transmitter, i.e., such that $\cos\phi_m < 0$. This can be motivated with the diffuse scattering from the rough surface which makes EM energy impinging on any target wall after reflection off the rough background surface. Indeed, the GW term exists if the target wall is illuminated by the plane wave raising after the reflection off the background surface and propagating in the direction $\hat{k}_{\mathrm{sg}}$, i.e., if

$$\hat{n}_{\mathrm{W}_m} \cdot \left(-\hat{k}_{\mathrm{sg}}\right) > 0\,, \tag{32}$$

or, given the specular reflection condition in (8), equivalently as

$$\hat{n}_{\mathrm{W}_m} \cdot \hat{k}_{\mathrm{s}} > 0\,, \tag{33}$$

that can be both rewritten as $\sin(\phi_s + \phi_m) > 0$.

The analytical expressions of the scattering matrix and scattering integral statistics are reported in Table 4 and Table 5 for the WG and GW contributions, respectively, where the local incidence angles on the mth wall ψ_m and $\overline{\psi}_m$ relevant to the WG and GW contributions, respectively, are evaluated as in (26) and as

$$\overline{\psi}_m = \cos^{-1}\left(-\hat{k}_{\mathrm{sg}} \cdot \hat{n}_{\mathrm{W}_m}\right), \tag{34}$$

respectively. Accordingly, in Table 5, $R_\perp^{\mathrm{W}}(\overline{\psi}_m) = R_\perp(\varepsilon_{\mathrm{r}}^{\mathrm{W}}, \overline{\psi}_m)$ and $R_{//}^{\mathrm{W}}(\overline{\psi}_m) = R_{//}(\varepsilon_{\mathrm{r}}^{\mathrm{W}}, \overline{\psi}_m)$. Within the GO-PO model, the local incidence angles on the ground relevant to the WG and GW terms coincide with the transmitter look angle θ as both $-\hat{k}_{\mathrm{sp}}$ and $-\hat{k}_{\mathrm{i}}$ share the same z-component, which is equal to $\cos\theta$.

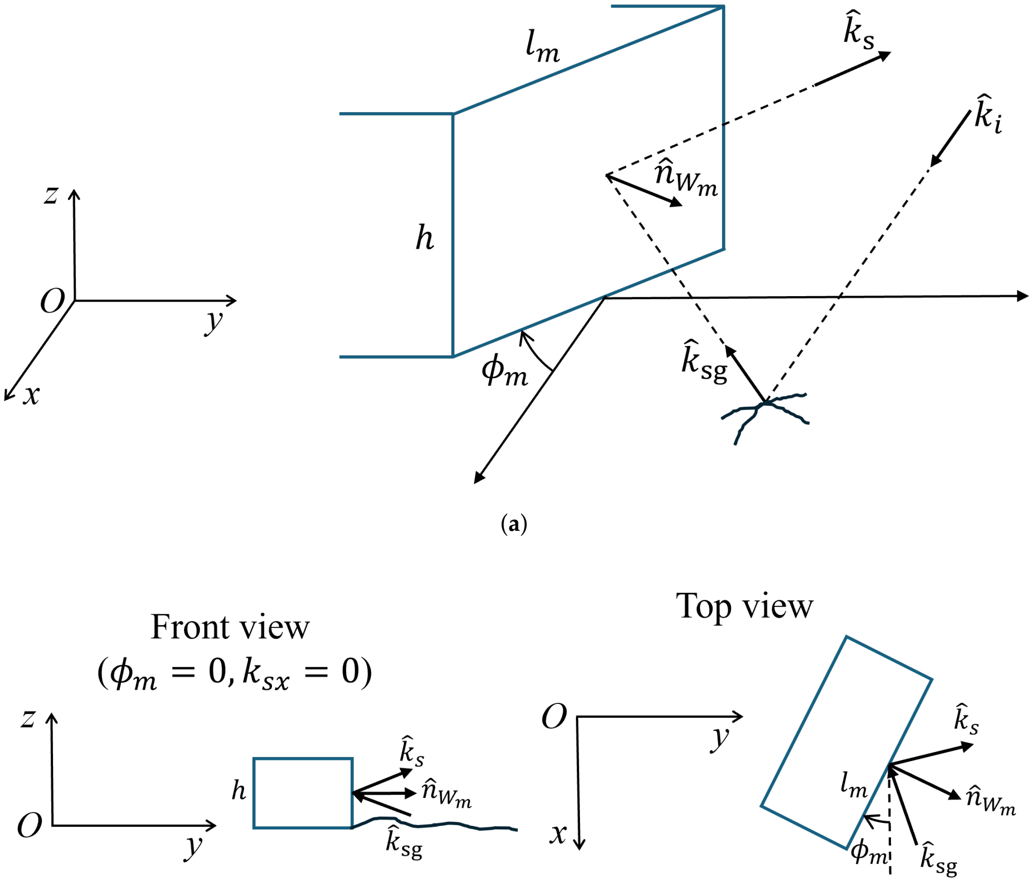

(**a**)

(**b**) (**c**)

Figure 5. GW scattering contribution. (**a**) 3-D view; (**b**) front view for $\phi_m = 0$ and $\hat{k}_{\mathrm{s}}$ lying in the $y - z$ plane; (**c**) top view.

Table 4. Double-scattering contribution (wall–ground).

$$S_{\mathrm{hh}} = \frac{2\sin\theta\cos\phi_m}{\sin^2\psi_m}\Bigg\{-\sin(2\phi_m+\phi_{\mathrm{s}})\left[R_\perp^{\mathrm{G}}(\theta)(\cos\theta+\cos\theta_{\mathrm{s}})+(\cos\theta_{\mathrm{s}}-\cos\theta)\right]\left[R_\perp^{\mathrm{W}}(\psi_m)\cos^2\theta\cos^2\phi_m-R_{//}^{\mathrm{W}}(\psi_m)\sin^2\phi_m\right]$$
$$-\cos(2\phi_m+\phi_{\mathrm{s}})\cos\theta\sin\phi_m\cos\phi_m\left[R_{//}^{\mathrm{G}}(\theta)(1+\cos\theta\cos\theta_{\mathrm{s}})+(1-\cos\theta_{\mathrm{s}}\cos\theta)\right]\left[R_\perp^{\mathrm{W}}(\psi_m)+R_{//}^{\mathrm{W}}(\psi_m)\right]\Bigg\}$$

$$S_{\mathrm{vh}} = \frac{2\sin\theta\cos\phi_m}{\sin^2\psi_m}\Bigg\{+\sin(2\phi_m+\phi_{\mathrm{s}})\cos\theta\sin\phi_m\cos\phi_m\left[R_\perp^{\mathrm{G}}(\theta)(\cos\theta+\cos\theta_{\mathrm{s}})+(\cos\theta_{\mathrm{s}}-\cos\theta)\right]\left[R_\perp^{\mathrm{W}}(\psi_m)+R_{//}^{\mathrm{W}}(\psi_m)\right]$$
$$-\cos(2\phi_m+\phi_{\mathrm{s}})\left[R_{//}^{\mathrm{G}}(\theta)(1+\cos\theta\cos\theta_{\mathrm{s}})+(1-\cos\theta_{\mathrm{s}}\cos\theta)\right]\left[R_{//}^{\mathrm{W}}(\psi_m)\cos^2\theta\cos^2\phi_m-R_\perp^{\mathrm{W}}(\psi_m)\sin^2\phi_m\right]\Bigg\}$$

$$\psi_m = \cos^{-1}(\sin\theta\cos\phi_m)$$

$$\langle I_{\mathrm{A}_0}\rangle = \mathrm{A}_0'\exp\left[-\frac{k^2\sigma^2}{2}(\cos\theta+\cos\theta_{\mathrm{s}})^2\right]\mathrm{sinc}\left[\frac{kl_m}{2}\left(\sin\theta\sin\phi_m-\sin\theta_{\mathrm{s}}\cos(\phi_{\mathrm{s}}+\phi_m)\right)\right]\mathrm{sinc}\left[\frac{kh\tan\theta}{2}\left(\sin\theta-\sin\theta_{\mathrm{s}}\sin(\phi_{\mathrm{s}}+2\phi_m)\right)\right]$$
$$\times\exp\Big\{jk\big[x_m(\sin\theta\sin 2\phi_m-\sin\theta_{\mathrm{s}}\cos\phi_{\mathrm{s}})+y_m(\sin\theta\cos 2\phi_m-\sin\theta_{\mathrm{s}}\sin\phi_{\mathrm{s}})\big]\Big\}\exp\left[\frac{jkh\tan\theta}{2}\left(\sin\theta-\sin\theta_{\mathrm{s}}\sin(\phi_{\mathrm{s}}+2\phi_m)\right)\right]$$

$$\sigma_{A_0}^2 = \exp\left(-k^2\sigma^2\eta_z'^2\right)\mathrm{A}_0'\sum_{n=1}^{+\infty}\frac{(k\sigma\eta_z')^{2n}}{n!}W^{(n)}(k\eta_x',k\eta_y')$$

$$\mathrm{COV}(I_{A_0}^{\mathrm{WG}},I_{A_0}^{\mathrm{GW}}) = \sigma_{A_0}^2\exp\left[2jk\eta_y'\left(\frac{\mathrm{A}_0'}{l_m}+x_m\sin(\phi_m)+y_m\cos(\phi_m)\right)\right]\mathrm{sinc}\left(k\eta_y'\frac{\mathrm{A}_0'}{l_m}\right)\qquad\text{if } \mathrm{A}_0'>0 \text{ and } \overline{\mathrm{A}}_0>0 \text{ (for } \overline{\mathrm{A}}_0 \text{ see Table 5)}$$

$$\mathrm{A}_0' = \begin{cases} l_m h\tan\theta\cos\phi_m, & \text{if } \cos\phi_m>0 \text{ and } \sin(\phi_{\mathrm{s}}+\phi_m)>0\\ l_m h[\tan\theta\cos\phi_m+\tan\theta_{\mathrm{s}}\sin(\phi_{\mathrm{s}}+\phi_m)], & \text{if } \cos\phi_m>0 \text{ and } \sin(\phi_{\mathrm{s}}+\phi_m)\le 0 \text{ and } \theta\ge\tan^{-1}\left(-\dfrac{\tan\theta_{\mathrm{s}}\sin(\phi_{\mathrm{s}}+\phi_m)}{\cos\phi_m}\right)\\ 0, & \text{otherwise}\end{cases}$$

$$\eta_x' = \sin\theta\sin\phi_m-\sin\theta_{\mathrm{s}}\cos(\phi_{\mathrm{s}}+\phi_m)$$
$$\eta_y' = \sin\theta\cos\phi_m-\sin\theta_{\mathrm{s}}\sin(\phi_{\mathrm{s}}+\phi_m)$$
$$\eta_z' = -\cos\theta-\cos\theta_s$$

The scattering areas relevant to the WG and GW contributions are proper projections of the target walls on the rough background surface as detailed in [20,22]. Indeed, they are the same as evaluated in the GO-GO bistatic model [22]. It is noteworthy that in Table 5, the expected value of the scattering integral $\langle I_{\mathrm{A}_0}\rangle$ must be evaluated as either $\langle I_{\mathrm{A}_0}\rangle_{\mathrm{ill}}$ if the mth target wall is illuminated (i.e., $\cos\phi_m > 0$) or as $\langle I_{\mathrm{A}_0}\rangle_{\mathrm{sh}}$ if it is shadowed (i.e., $\cos\phi_m < 0$).

Finally, the covariance between the double-bounce terms $\mathrm{COV}_m^{\mathrm{WG,GW}}$ can be written as

$$\mathrm{COV}_m^{\mathrm{WG,GW}} = \left(\frac{k}{4\pi r}\right)^2|E_{0p}|^2 S_{pq}^{\mathrm{WG}}S_{pq}^{\mathrm{GW}*}\mathrm{COV}(I_{A_0}^{\mathrm{WG}},\ I_{A_0}^{\mathrm{GW}}) \tag{35}$$

where the superscript * denotes the complex conjugate, while S_{pq}^{WG} and S_{pq}^{GW} stand for the pq entry of the scattering matrices relevant to the WG and GW terms, respectively, whose expressions are provided in Tables 4 and 5. The covariance between the scattering integrals $\mathrm{COV}(I_{A_0}^{\mathrm{WG}},\ I_{A_0}^{\mathrm{GW}})$ is reported in Table 4. It is worth mentioning that such a covariance is non-null only if both double-bounce terms are non-null. Notwithstanding, it is non-negligible only in limited scattering geometries, for which η_y' is sufficiently small (see Table 4). Remarkably, in backscattering $\eta_y' = 0$ regardless of the target orientation and, then, the covariance coincides with the variance of both double-bounce scattering terms. Actually, in this latter case, the double-bounce fields sum up coherently and the corresponding power is four times that of each double-bounce terms [20]. It is also worth noting that in the case of maximum correlation, i.e., $\eta_y' = 0$, the local incidence angles on the wall ψ_m and $\overline{\psi}_m$ coincide for both double-bounce terms (see Tables 4 and 5).

Table 5. Double-scattering contribution (ground–wall).

$$S_{\mathrm{hh}} = \frac{2\sin\theta_{\mathrm{s}}\sin(\phi_m+\phi_{\mathrm{s}})}{\sin^2\overline{\psi}_m}\Bigg\{ -\sin(2\phi_m+\phi_{\mathrm{s}})\Big[R_{\perp}^{\mathrm{G}}(\theta)(\cos\theta+\cos\theta_{\mathrm{s}})+(\cos\theta_{\mathrm{s}}-\cos\theta)\Big]\Big[R_{\perp}^{\mathrm{W}}(\overline{\psi}_m)\cos^2\theta_{\mathrm{s}}\sin^2(\phi_m+\phi_{\mathrm{s}})-R_{//}^{\mathrm{W}}(\overline{\psi}_m)\cos^2(\phi_m+\phi_{\mathrm{s}})\Big]$$

$$-\cos(2\phi_m+\phi_{\mathrm{s}})\cos\theta_{\mathrm{s}}\sin(\phi_m+\phi_{\mathrm{s}})\cos(\phi_m+\phi_{\mathrm{s}})\Big[R_{\perp}^{\mathrm{G}}(\theta)(1+\cos\theta\cos\theta_{\mathrm{s}})+(1-\cos\theta_{\mathrm{s}}\cos\theta)\Big]\Big[R_{\perp}^{\mathrm{W}}(\overline{\psi}_m)+R_{//}^{\mathrm{W}}(\overline{\psi}_m)\Big]\Bigg\}$$

$$S_{\mathrm{vh}} = \frac{2\sin\theta\sin(\phi_m+\phi_{\mathrm{s}})}{\sin^2\overline{\psi}_m}\Bigg\{ +\cos(2\phi_m+\phi_{\mathrm{s}})\Big[R_{//}^{\mathrm{G}}(\theta)(1+\cos\theta\cos\theta_{\mathrm{s}})+(1-\cos\theta_{\mathrm{s}}\cos\theta)\Big]\Big[R_{\perp}^{\mathrm{W}}(\overline{\psi}_m)\cos^2\theta_{\mathrm{s}}\sin^2(\phi_m+\phi_{\mathrm{s}})-R_{//}^{\mathrm{W}}(\overline{\psi}_m)\cos^2(\phi_m+\phi_{\mathrm{s}})\Big]$$

$$-\sin(2\phi_m+\phi_{\mathrm{s}})\cos\theta_{\mathrm{s}}\sin(\phi_m+\phi_{\mathrm{s}})\Big[R_{//}^{\mathrm{G}}(\theta)(\cos\theta+\cos\theta_{\mathrm{s}})+(\cos\theta_{\mathrm{s}}-\cos\theta)\Big]\Big[R_{\perp}^{\mathrm{W}}(\overline{\psi}_m)+R_{//}^{\mathrm{W}}(\overline{\psi}_m)\Big]\Bigg\}$$

$$\overline{\psi}_m = \cos^{-1}\left[\sin\theta_{\mathrm{s}}\sin(\phi_m+\phi_{\mathrm{s}})\right]$$

$$\langle I_{\mathrm{A}_0}\rangle_{\mathrm{ill}} = \overline{\mathrm{A}}_0\exp\left[-\frac{k^2\sigma^2}{2}(\cos\theta+\cos\theta_{\mathrm{s}})^2\right]\mathrm{sinc}\left[\frac{kl_m}{2}\Big(\sin\theta\sin\phi_m-\sin\theta_{\mathrm{s}}\cos(\phi_{\mathrm{s}}+\phi_m)\Big)\right]\mathrm{sinc}\left[\frac{kh\tan\theta_{\mathrm{s}}}{2}\Big(\sin\theta\sin\phi_{\mathrm{s}}+\sin\theta_{\mathrm{s}}\cos(\phi_{\mathrm{s}}+2\phi_m)\Big)\right]$$
$$\exp\Big\{-jk\big[x_m\sin\theta_{\mathrm{s}}\cos(\phi_{\mathrm{s}}+2\phi_m)+y_m(\sin\theta-\sin\theta_{\mathrm{s}}\sin(\phi_{\mathrm{s}}+2\phi_m))\big]\Big\}\exp\left[\frac{-jkh\tan\theta_{\mathrm{s}}}{2}\Big(\sin\theta\sin\phi_{\mathrm{s}}+\sin\theta_{\mathrm{s}}\cos(\phi_{\mathrm{s}}+2\phi_m)\Big)\right]$$

$$\langle I_{\mathrm{A}_0}\rangle_{\mathrm{sh}} = \langle I_{\mathrm{A}_0}\rangle_{\mathrm{ill}}\exp\left[-jkl_m(\sin\theta\cos\phi_m+\sin\theta_{\mathrm{s}}\sin(\phi_{\mathrm{s}}+\phi_m))\right]$$

$$\sigma_{A_0}^2 = \exp\left(-k^2\sigma^2\overline{\eta}_z^2\right)\overline{\mathrm{A}}_0\sum_{n=1}^{+\infty}\frac{(k\sigma\overline{\eta}_z)^{2n}}{n!}W^{(n)}(k\overline{\eta}_x,k\overline{\eta}_y)$$

$$\overline{\mathrm{A}}_0 = \begin{cases} l_m h\tan\theta_{\mathrm{s}}\sin(\phi_{\mathrm{s}}+\phi_m), & \text{if } \sin(\phi_{\mathrm{s}}+\phi_m)>0 \text{ and } \cos\phi_m>0 \\ l_m h[\tan\theta_{\mathrm{s}}\sin(\phi_{\mathrm{s}}+\phi_m)+\tan\theta\cos\phi_m], & \text{if } \sin(\phi_{\mathrm{s}}+\phi_m)>0 \text{ and } \cos\phi_m<0 \text{ and } \theta\le\tan^{-1}\left(-\dfrac{\tan\theta_{\mathrm{s}}\sin(\phi_{\mathrm{s}}+\phi_m)}{\cos\phi_m}\right) \\ 0, & \text{otherwise} \end{cases}$$

$$\begin{aligned} \overline{\eta}_x &= +\sin\theta\sin\phi_m-\sin\theta_s\cos(\phi_s+\phi_m) \\ \overline{\eta}_y &= -\sin\theta\cos\phi_m+\sin\theta_s\sin(\phi_s+\phi_m) \\ \overline{\eta}_z &= -\cos\theta-\cos\theta_s \end{aligned}$$

For better assessing the scattering geometries most impacted by such a correlation, Figure 6 shows 2-D graphs of the sinc term appearing in the covariance $\mathrm{COV}_m^{\mathrm{WG,GW}}$ for different orientation angles and relevant to a single target wall. As a matter of fact, the two double-bounce terms can be safely considered uncorrelated in most configurations, with the exception of those for which $\sin\theta_{\mathrm{s}}\sin(\phi_{\mathrm{s}}+\phi_m)$ is equal or sufficiently close to $\sin\theta\cos\phi_m$. It is useful to underline that the sinc term appearing in the covariance expression allows for a clear physical interpretation. It originates from the finite spatial extent of the effective scattering region contributing to both WG and GW double-bounce mechanisms. In particular, the kernel included in the covariance includes phase terms over a finite surface area, which leads to a sinc function related to the Fourier transform over a limited support. From a physical standpoint, this term controls the degree of coherence between the WG and GW contributions. When the phase difference between the two scattering mechanisms (i.e., the propagation paths) remains small over the illuminated area, the argument of the sinc function approaches zero and the covariance is maximized, indicating strong correlation. This always happens in the backscattering case, where the two propagation paths coincide exactly. Conversely, for increasing phase mismatch—driven by changes in geometry parameters such as incidence angle, scattering angle, or target orientation—the geometric decorrelation increases and coherence decreases.

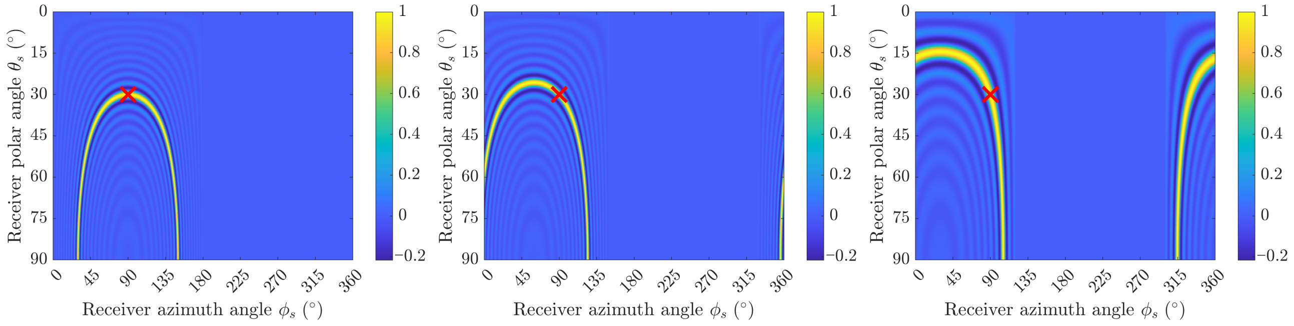

(**a**) (**b**) (**c**)

Figure 6. Sinc term of the covariance between the WG and GW scattering contributions (see Table 4) for (**a**) $\phi_1 = 0°$, (**b**) $\phi_1 = 30°$, and (**c**) $\phi_1 = 60°$. The look angle $\theta = 30°$, the frequency is 10 GHz, and the target has dimensions $l_1 = h = 1$ m. The red cross highlights the backscattering direction, namely $\theta_\mathrm{s} = 30°$ and $\phi_\mathrm{s} = 90°$ in this configuration.

3.3. Triple-Bounce Contributions

The triple-bounce WGW contributions are those scattering terms undergoing a double reflection from the target wall and a single reflection off the ground rough surface, see the yellow lines in Figure 2. This is the only triple-bounce scattering term arising in the considered scattering problem due to the assumed target geometry (i.e., smooth and vertical walls). Similarly to the WG term, the first reflection from the target wall gives rise to a plane wave propagating in the $\hat{k}_\mathrm{sp}$ direction, while, similarly to the GW term, the plane wave reaching the receiver is that propagating in the direction $\hat{k}_\mathrm{sg}$ after the reflection off the rough surface. Accordingly, the overall scattering matrix $\underline{\underline{S}}^\mathrm{WGW}$ relevant to the triple reflection can be evaluated as follows:

$$\underline{\underline{S}}^\mathrm{WGW} = \underline{\underline{S}}^\mathrm{W}(\hat{k}_\mathrm{sg}, \hat{k}_\mathrm{s})\underline{\underline{S}}^\mathrm{G}(\hat{k}_\mathrm{sp}, \hat{k}_\mathrm{sg}, \hat{z})\underline{\underline{S}}^\mathrm{W}(\hat{k}_\mathrm{i}, \hat{k}_\mathrm{sp}) \tag{36}$$

where $\hat{k}_\mathrm{sp}$ and $\hat{k}_\mathrm{sg}$ are provided in (28) and (30), respectively.

The scattering area is evaluated by following the approach in [22]. Remarkably, the area of the ground surface contributing to the triple-bounce scattering is evaluated as the intersection between two parallelograms (see Figure 7), namely those obtained by projection of the target wall on the ground surface along the $\hat{k}_\mathrm{sp}$ (green parallelogram) and the $\hat{k}_\mathrm{sg}$ (red parallelogram) directions. The former identifies the portion of ground impinged by the EM energy after the first reflection off the wall, while the latter identifies the portion of ground that might potentially contribute to the EM field at the receiver after the second reflection off the wall. Their intersection then provides the ground area actually contributing to the WGW term. The common area can be either a quadrilateral or a triangle, depending on the target and system geometry, as illustrated in Figure 7 and detailed in [22]. It is a quadrilateral if, in addition to (27) and (32), the following condition applies [22]

$$l_m > h m_y \left| \tan(\phi_m) - \cot(\phi_\mathrm{s} + \phi_m) \right| , \tag{37}$$

where m_y is reported in Table 6.

The analytical expressions of the scattering matrix and the scattering integral are reported in Table 6, where ψ_m and $\overline{\psi}_m$ stand for the local incidence angle on the wall at the first and second reflection, respectively, and are evaluated as in (26) and (34). It is worth noting that, in the limiting case of backscattering (i.e., $\theta_s = \theta$ and $\phi_\mathrm{s} = \pi/2$), $\psi_m = \overline{\psi}_m$, regardless of the target orientation angle.

Table 6. Triple-scattering contribution (wall–ground–wall).

$$S_{\mathrm{hh}}=\frac{4\sin\theta\sin\theta_{\mathrm{s}}\cos\phi_m\sin(\phi_m+\phi_{\mathrm{s}})}{\sin^2\psi_m\sin^2\overline{\psi}_m}\Big[T_{pp}(D'_{pp}+D''_{pp})-T_{pq}(D'_{qp}+D''_{qp})\Big]$$

$$S_{\mathrm{vh}}=\frac{4\sin\theta\sin\theta_{\mathrm{s}}\cos\phi_m\sin(\phi_m+\phi_{\mathrm{s}})}{\sin^2\psi_m\sin^2\overline{\psi}_m}\Big[T_{pp}(D'_{pq}+D''_{pq})+T_{pq}(D'_{qq}+D''_{qq})\Big]$$

$$T_{pp}=R_{\perp}^{\mathrm{W}}(\overline{\psi}_m)\cos^2\theta_{\mathrm{s}}\sin^2(\phi_m+\phi_{\mathrm{s}})-R_{//}^{\mathrm{W}}(\overline{\psi}_m)\cos^2(\phi_m+\phi_{\mathrm{s}})$$

$$T_{pq}=\Big[R_{\perp}^{\mathrm{W}}(\overline{\psi}_m)+R_{//}^{\mathrm{W}}(\overline{\psi}_m)\Big]\cos\theta_{\mathrm{s}}\sin(\phi_m+\phi_{\mathrm{s}})\cos(\phi_m+\phi_{\mathrm{s}})$$

$$D'_{pp}=\sin\phi_{\mathrm{s}}\Big[R_{\perp}^{\mathrm{G}}(\theta)(\cos\theta+\cos\theta_{\mathrm{s}})+(\cos\theta_{\mathrm{s}}-\cos\theta)\Big]\Big[R_{\perp}^{\mathrm{W}}(\psi_m)\cos^2\theta\cos^2\phi_m-R_{//}^{\mathrm{W}}(\psi_m)\sin^2\phi_m\Big],$$

$$D''_{pp}=-\cos\phi_{\mathrm{s}}\cos\theta\sin\phi_m\cos\phi_m\Big[R_{//}^{\mathrm{G}}(\theta)(1+\cos\theta\cos\theta_{\mathrm{s}})+(1-\cos\theta_{\mathrm{s}}\cos\theta)\Big]\Big[R_{\perp}^{\mathrm{W}}(\psi_m)+R_{//}^{\mathrm{W}}(\psi_m)\Big],$$

$$D'_{qp}=-\sin\phi_{\mathrm{s}}\cos\theta\sin\phi_m\cos\phi_m\Big[R_{//}^{\mathrm{G}}(\theta)(\cos\theta+\cos\theta_{\mathrm{s}})+(\cos\theta_{\mathrm{s}}-\cos\theta)\Big]\Big[R_{\perp}^{\mathrm{W}}(\psi_m)+R_{//}^{\mathrm{W}}(\psi_m)\Big],$$

$$D''_{qp}=-\cos\phi_{\mathrm{s}}\Big[R_{\perp}^{\mathrm{G}}(\theta)(1+\cos\theta\cos\theta_{\mathrm{s}})+(1-\cos\theta_{\mathrm{s}}\cos\theta)\Big]\Big[R_{\perp}^{\mathrm{W}}(\psi_m)\cos^2\theta\cos^2\phi_m-R_{//}^{\mathrm{W}}(\psi_m)\sin^2\phi_m\Big],$$

$$D'_{pq}=-\sin\phi_{\mathrm{s}}\cos\theta\sin\phi_m\cos\phi_m\Big[R_{\perp}^{\mathrm{G}}(\theta)(\cos\theta+\cos\theta_{\mathrm{s}})+(\cos\theta_{\mathrm{s}}-\cos\theta)\Big]\Big[R_{\perp}^{\mathrm{W}}(\psi_m)+R_{//}^{\mathrm{W}}(\psi_m)\Big],$$

$$D''_{pq}=-\cos\phi_{\mathrm{s}}\Big[R_{//}^{\mathrm{G}}(\theta)(1+\cos\theta\cos\theta_{\mathrm{s}})+(1-\cos\theta_{\mathrm{s}}\cos\theta)\Big]\Big[R_{//}^{\mathrm{W}}(\psi_m)\cos^2\theta\cos^2\phi_m-R_{\perp}^{\mathrm{W}}(\psi_m)\sin^2\phi_m\Big],$$

$$D'_{qq}=\sin\phi_{\mathrm{s}}\Big[R_{//}^{\mathrm{G}}(\theta)(\cos\theta+\cos\theta_{\mathrm{s}})+(\cos\theta_{\mathrm{s}}-\cos\theta)\Big]\Big[R_{//}^{\mathrm{W}}(\psi_m)\cos^2\theta\cos^2\phi_m-R_{\perp}^{\mathrm{W}}(\psi_m)\sin^2\phi_m\Big],$$

$$D''_{qq}=-\cos\phi_{\mathrm{s}}\cos\theta\sin\phi_m\cos\phi_m\Big[R_{\perp}^{\mathrm{G}}(\theta)(1+\cos\theta\cos\theta_{\mathrm{s}})+(1-\cos\theta_{\mathrm{s}}\cos\theta)\Big]\Big[R_{\perp}^{\mathrm{W}}(\psi_m)+R_{//}^{\mathrm{W}}(\psi_m)\Big],$$

$$\psi_m=\cos^{-1}(\sin\theta\cos\phi_m)$$

$$\overline{\psi}_m=\cos^{-1}[\sin\theta_{\mathrm{s}}\sin(\phi_m+\phi_{\mathrm{s}})]$$

$$\langle I_{A_0}\rangle=\frac{A}{2j}\exp\left[j(C+1)\frac{\tau_1+\tau_2}{2}\right](\tau_2-\tau_1)\left[\mathrm{sinc}\left((C+1)\frac{\tau_2-\tau_1}{2}\right)-\exp[-j(\tau_1+\tau_2)]\,\mathrm{sinc}\left((C-1)\frac{\tau_2-\tau_1}{2}\right)\right]$$

$$\sigma_{A_0}^2=\exp\left(-k^2\sigma^2\overline{\eta'_z}^2\right)\overline{\mathrm{A}'_0}\sum_{n=1}^{+\infty}\frac{(k\sigma\overline{\eta'_z})^{2n}}{n!}W^{(n)}(k\overline{\eta'_x},k\overline{\eta'_y})$$

$$A=-\frac{4}{k^2\overline{\eta'_x}^2m^-}\exp\left(-\overline{\eta'_z}^2\frac{k^2\sigma^2}{2}\right)\exp\left(jk\overline{\eta'_x}\frac{l_m}{2}\frac{m^+}{m^-}\right)\exp\left(jk\overline{\eta'_x}x'_m\right)\exp\left[jk\overline{\eta'_y}\left(y'_m+\frac{l_m}{m^-}\right)\right]$$

$$x'_m=x_m\cos\phi_m-y_m\sin\phi_m,\quad y'_m=x_m\sin\phi_m+y_m\cos\phi_m$$

$$C=-\frac{2\overline{\eta'_y}+\overline{\eta'_x}m^+}{\overline{\eta'_x}m^-},\quad \tau_1=\frac{k\overline{\eta'_x}}{2}l_m,\quad \tau_2=\frac{k\overline{\eta'_x}}{2}(l_m-Fm^-)$$

$$m_y=\min\big[\tan\theta\cos\phi_m,\tan\theta_{\mathrm{s}}\sin(\phi_{\mathrm{s}}+\phi_m)\big],\quad m^{\pm}=\big|\tan\phi_m\pm\cot(\phi_{\mathrm{s}}+\phi_m)\big|$$

$$F=\begin{cases}hm_y, & \text{if (37) holds}\\ \dfrac{l_m}{m^-}, & \text{otherwise}\end{cases}\qquad \overline{\mathrm{A}'_0}=F\left(l_m-\frac{F}{2}m^-\right)=\begin{cases}hm_y\left(l_m-\dfrac{hm_ym^-}{2}\right), & \text{if (37) holds}\\ \dfrac{l_m^2}{2m^-}, & \text{otherwise}\end{cases}$$

$$\begin{aligned}\overline{\eta'_x}&=+\sin\theta\sin\phi_m-\sin\theta_{\mathrm{s}}\cos(\phi_{\mathrm{s}}+\phi_m)\\ \overline{\eta'_y}&=+\sin\theta\cos\phi_m+\sin\theta_{\mathrm{s}}\sin(\phi_{\mathrm{s}}+\phi_m)\\ \overline{\eta'_z}&=-\cos\theta-\cos\theta_{\mathrm{s}}\end{aligned}$$

Finally, it must be noted that the triple-bounce WGW contribution exists if the target wall is directly illuminated by the plane waves propagating both in the $\hat{k}_{\mathrm{i}}$ and the $\hat{k}_{\mathrm{sg}}$ directions, i.e., if both (27) and (32) apply. Accordingly, the expressions of the coherent and incoherent components relevant to WGW reflection reported in Table 6 must be considered null if at least one between (27) and (32) does not hold.

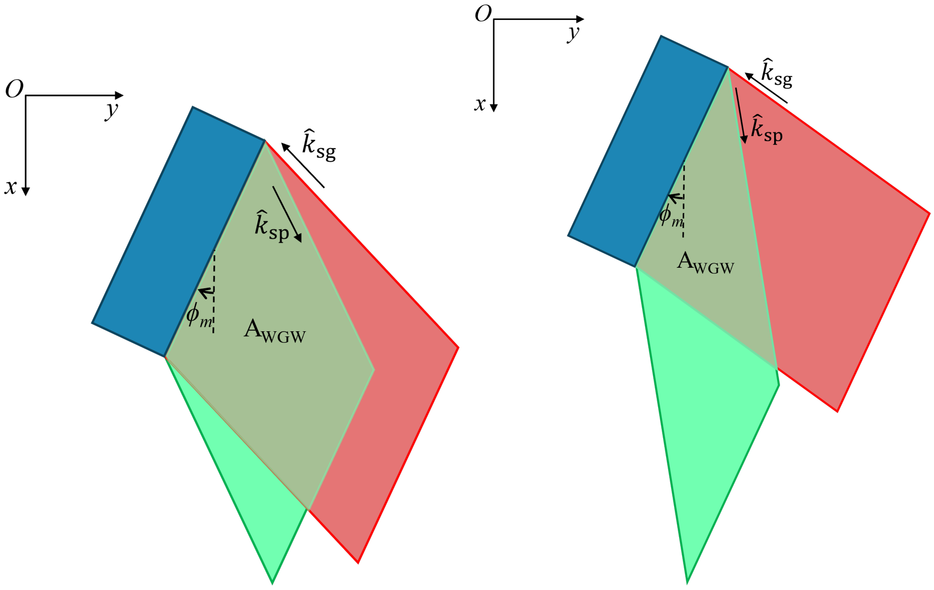

(**a**) (**b**)

Figure 7. Ground scattering areas contributing to the triple-bounce term WGW in the (**a**) quadrilateral case, (**b**) triangle case. The area contributing to the WGW term is the intersection between the red and green parallelograms.

3.4. Model Overview

To facilitate readability of the derivation procedure and the reproducibility of the proposed model, we summarize here the main derivation steps leading from the general scattering formulation reported in Section 2.1 to the closed-form expressions reported in Tables 4–6. Indeed, here we focus on the derivation of multiple-bounce terms, being single reflections from rough and smooth surface using KA well-assessed topics in microwave scattering theory.

The analytical expressions reported in Tables 4–6 are derived starting from the general formulation of the scattered field given in (6)–(7), by specifying, for each scattering mechanism, the corresponding scattering matrix and scattering integral.

More specifically, the scattering matrix relevant to the multiple-bounce terms is constructed by proper combination of the elementary reflection contributions from the rough ground and the target walls. In particular, the overall scattering matrix is obtained as the product of the matrices associated with each single reflection, according to (29), (31), and (36) for the WG, GW, and WGW contributions, respectively. For scattering matrix evaluation, it is useful to recall that the input vectors $\hat{k}_{\mathrm{i}}$, $\hat{k}_{\mathrm{s}}$, $\hat{k}_{\mathrm{sp}}$, and $\hat{k}_{\mathrm{sg}}$ are defined in (3), (4), (28), and (30), respectively.

The scattering integral I_{A0} is evaluated by identifying, for each scattering mechanism, the phase term through the appropriate difference vector and the corresponding scattering area, that accounts for the effective ground area illuminated by both the transmitter and the receiver. These quantities depend on the specific interaction geometry and are explicitly reported in the bottom part of Tables 4–6. In particular, they are identified as A_0' and $\underline{\eta}'$, $\overline{A}_0$ and $\overline{\underline{\eta}}$, $\overline{A'}_0$ and $\overline{\underline{\eta}'}$, for WG, GW, and WGW terms, respectively. Once such replacements have been performed, the scattering integral statistics, i.e., mean and variance, can be computed in a way similar to the single-reflection term.

The relative importance of the different scattering mechanisms depends on both the acquisition geometry and the surface roughness. A qualitative summary is provided in Table 7.

Table 7. Qualitative dominance of the main scattering mechanisms.

Scattering Mechanism	**Main Characteristics**
Ground (single)	Single reflection from gound: near-specular reflection; the smoother the surfaces, the stronger the contribution
Target roof (single)	Single reflection from target roof: specular reflection; dominates in the specular reflection in presence of rough ground; practically negligigle in far-from-specular directions
Target Wall (single)	Single reflection from target walls: weak except near grazing angles; can be assumed negligible in practical remote sensing applications
WG and GW	Double bounce ground–wall (GW) and wall–ground (WG): dominate over single- and triple-bounce terms in the backscattering region; they coincide in amplitude and phase only in the backscattering direction; stronger and more directive for smoother ground surfaces
WGW	Triple reflection wall–ground–wall: strong near backscattering; weaker than double-bounce terms; stronger and more directive for smoother ground surfaces

4. Results and Discussion

In this section, we provide some comparisons of our GO-PO bistatic scattering model with other models, numerical tools, and measurements available in the literature. Model input parameters are reported in Tables 8 and 9 for the different scenarios analyzed, where an isotropic Gaussian-correlated background surface has been assumed. To provide quantitative information about the applicability of the proposed model, we also report the rms slope, that can be evaluated as $2\sigma/l_c$ for the Gaussian ACF. In all the considered test cases, the rough surface rms slope is lower than 0.25, but for the last scenario. As follows in this section, the ground, the target, and the composite RCSs are evaluated according to the proposed GO-PO model as detailed in Section 3.

Table 8. GO-PO model input parameters for validation with numerical/hybrid solvers.

	Figure 8a	**Figure 8b**	**Figure 9**	**Figure 10**
Frequency	10 GHz	10 GHz	3 GHz	10 GHz
Look angle	varying	45°	40°	40°
Diel. const. (target)	Aluminum [30]	Aluminum [30]	$4.45 + j2.72 \times 10^7$	$4.45 + j2.72 \times 10^7$
Diel. const. (ground)	Aluminum [30]	Aluminum [30]	$70.07 + j40.19$	$72.10 + j90.13$
Rough surf. std. dev. (σ)	0	0	7.6 mm	67 mm
Rough surf. corr. length (l_c)	12.8 µm	12.8 µm	86.4 mm	1.68 m
Rough surf. RMS slope	0	0	0.176	0.080
Target size ($l_1 \times l_2 \times h$)	$6 \times 6 \times 6$ cm^3	$6 \times 6 \times 6$ cm^3	$120 \times 20 \times 10$ m^3	$31.6 \times 4.3 \times 5$ m^3
Target orientation (ϕ_1)	0°	0°	0°	0°
Polarization	VV	VV	HH	VV

Table 9. GO-PO model input parameters for validation with measurements.

	Figure 11a	**Figure 11b**	**Figure 11c**	**Figure 12**
Frequency	9.65 GHz	9.65 GHz	9.65 GHz	8 GHz (a); 14 GHz (b)
Look angle	52.25°	52.25°	52.25°	0°
Diel. const. (target)	$8.0 + j0.5$	$8.0 + j0.5$	$4.0 + j0.05$	Aluminum [30]
Diel. const. (ground)	$8.0 + j0.5$	$8.0 + j0.5$	$14.0 + j.01$	Aluminum [30]
Rough surf. std. dev. (σ)	1.4 mm	1.4 mm	10 mm	0
Rough surf. corr. length (l_c)	1.8 cm	1.5 cm	5.5 cm	10 μm
Rough surf. RMS slope	0.156	0.187	0.364	0
Target size ($l_1 \times l_2 \times h$)	$\frac{1.1}{\cos(\phi_1)} \times 0 \times 6.5$ m^3	$\frac{1.1}{\cos(\phi_1)} \times 0 \times 6.5$ m^3	$\frac{1.1}{\cos(\phi_1)} \times 0 \times 6.5$ m^3	$280.5 \times 240.6 \times 1.8$ mm^3
Target orientation (ϕ_1)	varying	varying	varying	0
Polarization	HH	HH	HH	-

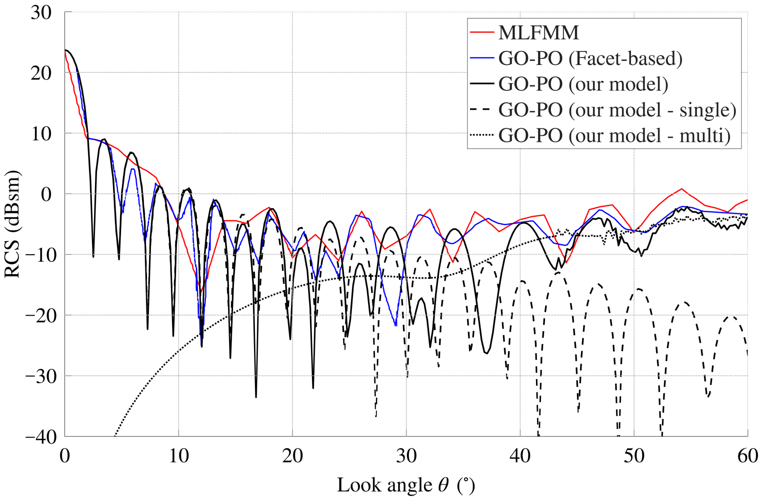

(**a**)

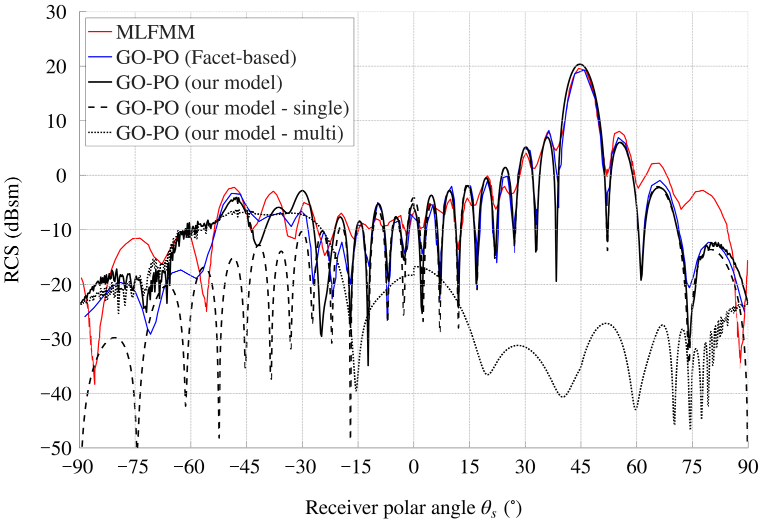

(**b**)

Figure 8. Comparison of our GO-PO model (black lines) with the MLFMM (red line) and the facet-based GO-PO (blue line) described in [16]. GO-PO (facet-based) and MLFMM comparison results are taken from (**a**) ([16] Figure 8a) and (**b**) ([16] Figure 8b). Concerning our GO-PO model, in addition to the overall RCS (black solid line), we also show the single-bounce RCS (black dashed line), and the multiple-bounce RCS (black dotted line) evaluated according to Section 3.

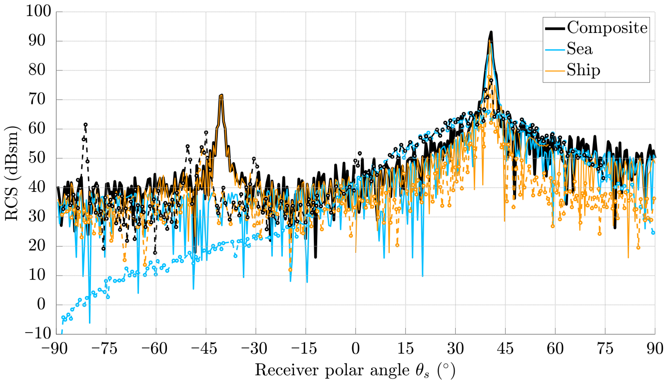

Figure 9. Comparison of our GO-PO model (solid lines) with the results in([17] Figure 7a) (dashed lines with circles) relevant to ship (orange), sea (cyan), and total (black) RCS. For the sake of conciseness, the legend explains only color association.

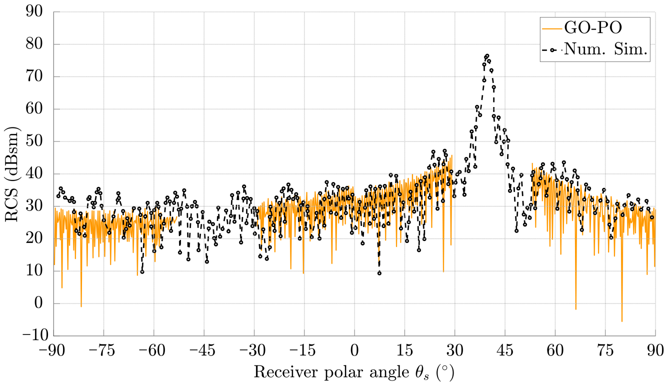

Figure 10. Comparison of our GO-PO model (solid orange line) with the numerical simulation results in ([18] Figure 16) (dashed black line with circles) relevant to ship RCS.

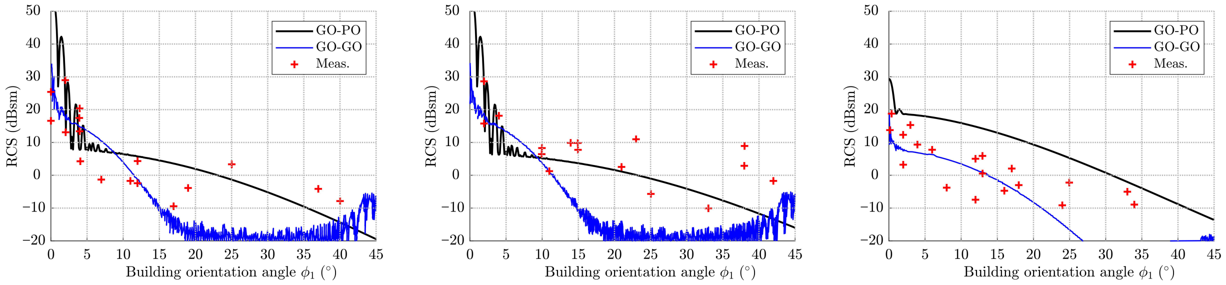

(**a**) (**b**) (**c**)

Figure 11. Comparison of our GO-PO model (black line) with the monostatic measurements provided in [21] (red crosses) and the companion GO-GO model (blue line) in different scenarios, namely (**a**) residential buildings over asphalt, (**b**) industrial buildings over asphalt, and (**c**) residential buildings over grass-covered soil. Measurements have been extracted from ([21] Figure 2).

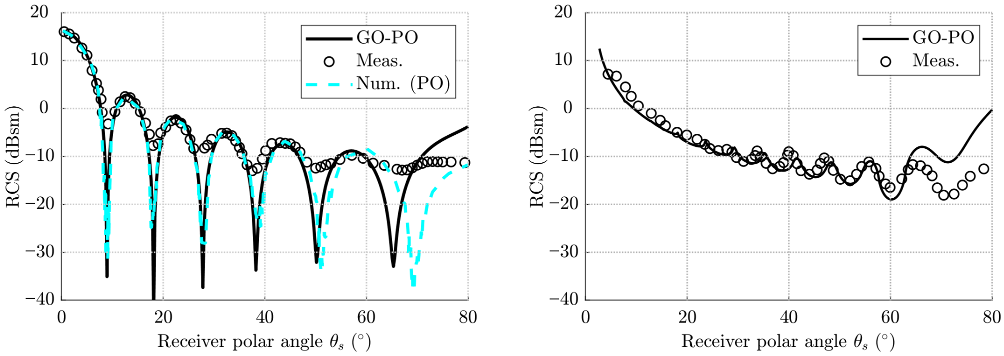

(**a**) (**b**)

Figure 12. Bistatic RCS of a thin metallic plate at (**a**) 8 GHz, and (**b**) 14 GHz. GO-PO (black solid line), measurements (black circles), numerical PO (cyan dashed line).

Remarkably, we compare the proposed analytical GO-PO bistatic scattering model with the numerical hybrid approaches discussed in [16–18] and with the measurements presented in [21,31] relevant to backscattering and bistatic scattering geometries, respectively.

Additionally, it is worth mentioning that the subsequent analyses are carried out by assuming an isotropic ground surface, even though the proposed model can deal with surface anisotropy via the nth-order power spectrum $W^{(n)}(\cdot,\cdot)$ that can be set according to the closed-form formulas in Table 1 or be numerically evaluated from any arbitrary surface spectrum as discussed in Section 2.2.

Finally, a last remark about computational efficiency of the proposed GO-PO model. Compared to full-wave or numerical/hybrid methods, fully analytical models, such as the proposed GO-PO, exhibit, possibly, much higher computational efficiency due to the absence of computationally demanding numerical integration. Notwithstanding, compared to other closed-form models, such as GO-GO or GO-SPM, the proposed GO-PO model still requires the evaluation of the series appearing in the scattering integral variance (as reported in Tables 2–6). This leads to a relatively increased computational complexity compared to other analytical methods (e.g., GO-GO), even though it remains well below that of numerical/hybrid approaches. Indeed, the GO-PO results relevant to the test cases analyzed in the subsequent Sections 4.1 and 4.2, where a Gaussian ACF is assumed due to the lack of adequate information in the relevant literature, are obtained in few seconds with a common workstation (16 GB RAM, i7 9750H). In the case a closed-form expression of the nth-order power spectrum is not available, the computational complexity may significantly increase due to the numerical evaluation of the nth-order power spectrum from the surface roughness ACF via (11). Finally, if the rough surface statistics are provided by means of its surface power spectral density (as it is typically the case for sea surface), a further numerical integration step is required in order to evaluate first the surface ACF via (12). In the case that numerical evaluation of the nth-order power spectrum is required, the evaluation of the scattered field for a large amount of observation/incidence directions can be sped-up by construction of look-up tables of the $W^{(n)}(k_x, k_y)$ function. This preliminary step is undertaken once for all and takes few minutes on a common workstation. Finally, it is worth noting that the infinite series appearing in the variance of the scattering integral exhibits fast convergence in most practical configurations within the validity range of the PO approximation. In addition, convergence acceleration techniques, such as the Shanks transformation, can be employed to further improve numerical efficiency when needed [32].

4.1. Comparison with Numerical Solvers

In this section, we provide some comparisons with different numerical solvers developed to deal with the scattering problem in the scenarios of interest in our work. First, we consider the results reported in [16], where the composite scattering from complex targets over a rough surface is evaluated by means of a facet-based GO-PO asymptotic model. However, in [16], the nomenclature GO-PO is used to refer to a combination of ray tracing and PO to determine scattering from the facets belonging to either the rough surface or the target and, hence, our approach is rather different as GO is adopted for scattering from the target walls and PO to scattering from the rough surface. Additionally, our GO-PO model is fully analytical (at least for the surface types reported in Table 1), i.e., the scattered-field statistics are expressed via algebraic functions of both system and scene parameters. Accordingly, neither ray-tracing nor numerical solvers are required, even though simplified target geometries can be analyzed.

Figure 8 compares the results obtained with our model (black lines) with those shown in ([16] Figure 8a) and ([16] Figure 8b), respectively, (blue line) which are relevant to scattering from a perfect electric conductor (PEC) cube on a PEC square plane in backscattering (Figure 8a) and bistatic scattering (Figure 8b). The results obtained in [16] through the multilevel fast multi-pole method (MLFMM) are reported as well for further comparisons (red line). In this simplified geometry, our model (solid black line) exhibits a good agreement with both numerical models showing only slight discrepancies in the backscattering case for θ ranging from 30° to 40°. In backscattering (Figure 8a), the overall RCS is dominated by the single-scattering contributions from the target roof and the background plane for low look angles (see the black dashed line), whereas, for increasing look angles, the multiple-bounce terms are the dominant contributions (see the dotted line), as also noted in [16]. Figure 8b shows results for in-plane bistatic scattering, i.e., for scattering directions lying in the incidence plane, that, in the reference system adopted here, coincides with the yz plane.

In accordance with [16], negative values of θ_s correspond to $\phi_s = \pi/2$ (backward region), while the positive ones to $\phi_s = 3/2\pi$ (forward region). In such a geometry, the peak of the overall (i.e., target, surface, and coupling) RCS is measured in the forward-scattering direction, i.e., for $\theta_s = 45^\circ$, where specular scattering from single-bounce terms dominates (see black dashed line). Conversely, the multiple-scattering contributions dominate in backscattering, leading to RCS enhancement around $\theta_s = -45^\circ$ (see black dotted line). It is worth emphasizing that the facet-based GO-PO approach in [16] is a hybrid high-frequency method based on surface discretization and ray-tracing techniques, which are required to model shadowing effects and multiple interactions. While this approach can provide accurate predictions for complex geometries, it does not lead to closed-form expressions and, therefore, is poorly suited to parametric analysis and offers limited physical insight into the dependence of the scattered field on the scene parameters.

In contrast, the proposed analytical GO–PO model provides explicit algebraic expressions for the different scattering contributions, enabling both a direct interpretation of the underlying mechanisms and a significantly reduced computational cost. Accordingly, the two approaches should be regarded as complementary rather than competitive, their use depending on the specific application requirements.

Second, we compare our results with those reported in [17], where scattering from the target and the rough surface is evaluated numerically through a facet-based approach and by using a combination of GO and Bass–Fuks two-scale model, while the method of equivalent current is adopted along with a combination of the four-path model [33] and the quasi-image method to calculate the target-surface coupling, i.e., the multiple bounces. Figure 9 compares the ship (orange), sea (cyan), and overall (black) RCSs evaluated according to our model (solid lines) with the results shown in ([17] Figure 7a) (dashed lines with circles), which are relevant to a realistic ship with slightly tilted walls and superstructures, see ([17] Figure 7a). The results shown in Figure 9 refer to in-plane scattering with the same convention as in Figure 8b about the sign of θ_s. As emerges from Figure 9, our model predicts a secondary peak in the backscattering direction (i.e., $\theta_s = -40^\circ$ in this case) due to the multiple-bounce scattering, i.e., the EM coupling between the sea surface and the vertical ship walls. Conversely, as mentioned above, the target model considered in [17] includes geometrical details such as superstructures and walls slightly tilted both downwards and upwards, which are not accounted for in our simplified model. These features can generate additional multiple-reflection contributions, leading to the secondary peaks observed in Figure 9, especially in the backward region. More specifically, in the backward region, two separate peaks emerge in directions slightly lower (downwards walls) and higher (upwards walls) than the backscattering one. In the forward region, our model predicts larger RCS due to the much larger ship deck (target plane roof), that, in the model considered in [17], is instead mostly occupied by superstructures. Notwithstanding, despite the much larger complexity of the target model considered in [17], the GO-PO model exhibits a reasonable overall agreement with the more computationally demanding numerical solver.

Then, we consider the EM solver described in [18], which is a facet-based numerical method using KA combined with the graphical EM computing method to evaluate illuminated and shadowed facets; EM coupling between the target and the rough surface is evaluated by means of the four-path model [33]. As in [17], also the target considered in [18] is a complex ship model with a curved hull and fine superstructures above the ship deck, see ([18] Figure 15). Unfortunately, this scenario does not fit well with the validity limits of PO. Indeed, as discussed in Section 2.1, the zeroth-order PO requires, among other hypotheses, that $k\sigma|\eta_z|$ be sufficiently small (theoretically $k\sigma|\eta_z| \ll 1$, practically $k\sigma|\eta_z| \lesssim 1$). This condition is clearly not satisfied in the problem considered in [18], where

$k\sigma|\eta_z|$ varies in the range 10–25 over the whole range of θ_s, see simulation parameters in Table 8. Indeed, this case study refers to a simulation setup characterized by a large roughness and high $k\sigma$. Under this scenario, the power series in the scattering integral variance converges very slowly and becomes numerically unstable, since a large number of terms would be required for an accurate evaluation. This effect is particularly evident for scattering directions close to backscattering and forward-scattering (i.e., for $|\theta_s| \approx \theta$), where the numerical evaluation of the power series becomes unreliable. As a consequence, the series representation reported in Tables 2–6 is no longer practically convergent in those regions. Notwithstanding, we recall here that in the case of large $k\sigma$, the companion GO-GO model can be used. For the above considerations, in Figure 10 we show only finite values of the ship RCS evaluated according to our GO-PO model (solid orange line) and compare them with the corresponding simulation results reported in ([18] Figure 16). Notwithstanding, it should be noted that, even considering this challenging scenario, the GO-PO model fits reasonably well the numerical solver in predicting the EM behavior of the target coupled with the rough background surface. It is also worth mentioning that the large sea surface roughness of the composite scene considered in [18] fits better the validity limits of the complementary GO-GO model described in [22], that, indeed, allows for computing the field scattered in any direction and, in fact, is in good agreement with the simulation results in [18] for ship, sea, and composite scattering, see ([22] Figure 5).

4.2. Comparison with Measurements

In this section, we provide some comparisons with RCS measurements of parallelepiped-like targets acquired both in monostatic and bistatic geometries.

Figure 11 shows comparisons with the backscattering measurements provided in [21], where the RCS of a large number of buildings with varying orientations is extracted from a pair of spotlight TerraSAR-X images acquired in HH polarization on the city of Dorsten, Germany. The spatial resolutions are 1.1 m and 1.2 m in azimuth and slant range, respectively, while the incidence angles are 50.7° and 53.8° for the two acquisitions. The considered building dataset comprises different types of scenarios, including residential buildings over asphalt terrain (Figure 11a), industrial buildings over asphalt terrain (Figure 11b), and residential buildings over grass-covered soil (Figure 11c) [21]. The geometric and dielectric properties of the buildings and ground have been derived in [21] by means of an optimization procedure aimed at best fitting an analytical GO-SPM backscattering model with the measurements extracted from the SAR images. All the model input parameters are listed in Table 9 and are taken from [21]. As the measurements have been derived by combining the returns from both images, here we consider an average look angle of 52.25°. Additionally, the authors in [21] focused on the analysis of the SAR double-bounce line, which is contributed by an horizontally limited portion of a single building wall whose length must account for both the azimuth resolution and the building orientation. This leads to the building dimensions setup as reported in Table 9. Accordingly, RCS evaluations have been performed by considering only the WG and GW double-bounce terms. In this test case, we compare the GO-PO model proposed here with the measurements extracted from [21] and with the companion GO-GO model presented in [22] to better highlight the complementary applicability of the two analytical models. Figure 11 reveals that the GO-PO model exhibits a good agreement with the measurements in the first two test cases where the buildings are placed over asphalt terrain, see Figure 11a,b, whereas a slight overestimation can be observed in the residential/grass case, see Figure 11c. On the other hand, the GO-GO model provides worse accuracy in the asphalt terrain cases, especially for intermediate orientation angles, whereas it overcomes GO-PO in the grass-covered soil. Such results are in accordance with the expected applicability of the two models. Indeed, in the asphalt terrain cases, the ground rms slope is very low (see Table 9), whereas the surface roughness standard deviation is not much larger than wavelength. Conversely, in the grass-covered soil case, rms slope is larger than 0.25, whereas the surface roughness standard deviation is significantly larger than wavelength. Consequently, PO is expected to provide better accuracy than GO in the first two test cases, and GO is expected to be more accurate than PO in the third one. The results in Figure 11 also highlight that both the GO-PO and GO-GO models exhibit lower accuracy for large orientation angles. This is likely due to the fact that in such observation configurations, the multiple reflection terms contributing to backscattering are related to out-of-plane scattering from the rough ground, where both models are less accurate. It is also worth noting that the grass-covered soil test case in Figure 11c could be characterized by non-negligible volume scattering from grass at the considered operating frequency of 9.65 GHz. However, volume scattering is not expected to be the dominant contribution compared to multiple bounces, especially in the monostatic geometry (analyzed in this case study) and for buildings facing the radar, i.e., for low building orientation angles. Indeed, the companion GO-GO model provides good agreement with measurements, at least for orientation angles up to 25°.

To further assess the accuracy of the proposed GO-PO model in a real bistatic configuration, we examined the experimental data presented in [31]. There, the bistatic RCS of a thin metallic plate positioned above a smooth metallic ground plane was measured at 8 GHz and 14 GHz under normal incidence condition ($\theta = 0$), with both transmitter and receiver aligned along the plate's long edge. The corresponding geometric and operational parameters are provided in Table 9. It is worth noting that our method requires a statistical description of a rough ground surface, whereas the measurements in [31] were carried out over a smooth metallic plate. To reproduce this scenario, both the surface height standard deviation and correlation length were therefore set according to typical metallic surface roughness [34], see Table 9. The results are reported in Figure 12 for (a) 8 GHz and (b) 14 GHz and show the bistatic RCS evaluated according to our model (black solid line), field measurements (black circles), and a numerical PO solver (cyan dashed line) described in [31]. The imaging and geometric conditions of this test case cause the single-scattering contribution from the plate to dominate over the multiple-reflection terms. This is consistent with the characteristic sinc-like pattern visible in Figure 12. Overall, our closed-form model exhibits a good agreement with the measurements up to θ_s values as large as 60°, from which it deviates significantly from measured data, likely due to the near grazing incidence. Additionally, the estimations obtained with the proposed approach are nearly indistinguishable from those produced by the numerical PO solver employed in [31], further demonstrating the correctness of the proposed methodology.

4.3. Validity Limits

The applicability of the proposed GO-PO model is inherently tied to the validity conditions of the KA and of its GO and zeroth-order PO solutions, that are studied in classical textbooks on microwave scattering from random rough surfaces, e.g., [8,35,36].

First, KA requires that the mean radius of curvature of the scattering surface be much larger than the wavelength and that shadowing and multiple reflections over the same surface are negligible. These conditions typically impose low-to-moderate incidence and scattering angles (e.g., $\theta, \theta_s \lesssim 60°$).

The GO approximation is adopted only for the target walls, which are assumed to be smooth and electrically large. Under these conditions, the scattered field can be accurately described as a single plane wave propagating in the specular direction. Accordingly, no roughness-related constraints (e.g., on $k\sigma$) apply to the target contribution.

Conversely, the rough background surface is modeled through the zeroth-order PO approximation, which introduces additional constraints. In particular, PO requires the surface being gently to moderately rough, i.e., characterized by small local slopes (typically rms slope lower than 0.25), and that the parameter $k\sigma|\eta_z|$ be sufficiently small to ensure practical convergence and reliability of the power series appearing in the scattering integral variance.

From a practical standpoint, the zeroth-order PO approximation is reliable when $k\sigma|\eta_z| \lesssim 1$, and may lead to slow convergence and numerical instability for larger values (approximately $k\sigma|\eta_z| \gtrsim 3$). In such cases, higher-order approximations or the companion GO-GO model are more appropriate.

A schematic representation of the validity limits of the proposed GO-PO model are summarized in Table 10.

In summary, the proposed GO-PO formulation is best suited for scenarios involving electrically large, smooth, and parallelepiped-like targets over mildly rough surfaces (e.g., calm to moderate sea or smooth terrain). Its accuracy degrades in the presence of highly rough surfaces, large values of $k\sigma|\eta_z|$, high incidence and/or scattering angles, moderate-to-dense vegetation.

To further clarify the applicability of the proposed formulation and its relationship with the companion GO-GO model, we report a qualitative map of the validity domains of GO and PO for ground scattering modeling in Figure 13.

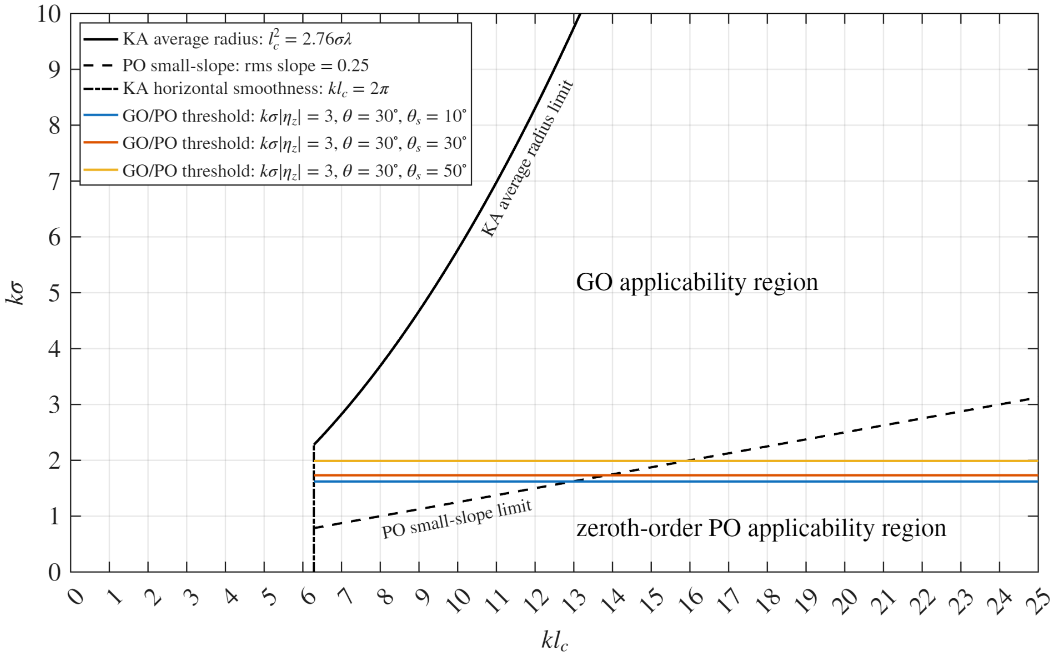

Figure 13. Applicability domains of the GO and PO formulations for ground scattering as a function of the normalized roughness parameters kl_c and $k\sigma$. The curves represent the validity conditions for KA, GO, and zeroth-order PO.

The diagram is expressed in terms of the normalized roughness parameters $k\sigma$ and kl_c, and includes the main constraints associated with the KA, the zeroth-order PO, and the GO solutions, that are also mentioned in Table 10. In particular, the condition $k\sigma|\eta_z|$ is used to highlight the transition between zeroth-order PO and GO regimes, while the constraints on kl_c and surface curvature identify the domain where the general KA-based framework is applicable.

The figure shows that the GO-PO and GO-GO models operate in largely complementary regions of the roughness parameter space. The GO-PO formulation is suited for mildly rough surfaces with small slopes and moderate values of $k\sigma$, whereas the GO-GO model becomes more appropriate for very rough surfaces characterized by large $k\sigma$. Accordingly, the proposed GO-PO model should be regarded as a complementary extension, rather than as a direct alternative, of the GO-GO formulation.

Table 10. Validity conditions of the proposed GO–PO model.

Component	Model	Requirement	Condition
General framework	KA	Tangent plane approximation Negligible shadowing/reflections	$l_c^2 > 2.76\sigma\lambda$ $\theta, \theta_s \lesssim 60°$
Target walls	GO	Smooth and electrically large surfaces	$h, l_m \gg \lambda$
Ground	PO	Small local slopes	rms slope $\lesssim 0.25$
PO series	–	Convergence of power series	$k\sigma\|\eta_z\| \lesssim 1$

5. Conclusions

In this paper, we have presented an analytical model for the EM scattering from a composite scene comprising a parallelepiped target lying over a random rough background surface. Closed-form expressions for the coherent and incoherent components of the single- and multiple-bounce scattering contributions arising from the EM interaction between the target walls and the rough surface have been derived within the framework of KA. Remarkably, the GO and PO solutions are adopted for describing the EM behavior of the smooth, and possibly lossy, target walls and the rough ground, respectively. More generic expressions have been derived assuming a rough surface with an arbitrary power spectrum, hence including anisotropic surfaces, and have been specialized for surfaces, possibly anisotropic, with Gaussian or exponential correlation. The derived algebraic formulas allow to express the overall scattered-field strength as a function of the main system and scene parameters, e.g., frequency, polarization, incidence and scattering angles, target size, composition, and orientation. The proposed model is fully analytic and, as such, it does not require any facet decomposition, numerical integrations, Monte Carlo simulations, or measurements calibration to determine the target RCS.

Comparisons with other numerical EM solvers and measurements available in the literature have shown reasonable accuracy of the proposed model in predicting the bistatic RCS of complex targets, including ships and buildings. Remarkably, in accordance with the literature, our model predicts an RCS enhancement in the backward region due to the multiple reflections between the rough ground and the target walls, which act like a mirror.

The proposed model provides an EM tool which is complementary to numerical solvers: the former assumes a simplified target geometry and can provide fast and reasonable estimations of the overall field scattered from the composite scene, whereas the latter can simulate arbitrary target models at the cost of a possibly much larger computational complexity. As a further relevant distinction, our analytical approach can provide physical insights into the role of the main scene parameters involved into the scattering problem and is more suited to the design of efficient inversion methods, such as the estimation of geophysical or target parameters. Notwithstanding, the proposed approach relies on a simplified target geometry and, hence, cannot describe the EM response of fine structural details, such as windows and superstructures. However, as it has been demonstrated, the model can describe with reasonable accuracy the main scattering mechanisms, including the multiple reflections arising from the EM interaction between the target and the surrounding rough surface. Additionally, the modeling of the ground surface scattering via the PO solution makes the proposed formulations unreliable in presence of moderate-to-very rough backgrounds. However, in such ground roughness conditions, the companion GO-GO model could be adopted. Indeed, it is worth emphasizing that the proposed GO-PO formulation is not intended as a direct alternative to the companion GO-GO model.

Rather, the two approaches are complementary and address different roughness regimes, as demonstrated in this work. The GO-PO model is particularly suited for mildly rough surfaces, where the PO approximation provides a more accurate description of the ground scattering. Conversely, the GO-GO formulation remains more appropriate for moderate-to-very rough surfaces. In this sense, the proposed model extends the bistatic analytical framework by filling a gap not covered by the GO-GO approach.

The formulations provided here may be exploited in urban (e.g., buildings) and maritime (e.g., ships) domains, where potential applications might include bistatic remote sensing systems design and analysis, target detection and discrimination, scene parameters retrieval from bistatic microwave remote sensing data.

The analyses provided here might also support a correct human interpretation and automatic processing of urban bistatic SAR images, possibly leveraging machine learning paradigms. An example is reported in [37], where the proposed model was exploited to investigate the so-called *cardinal effect* in bistatic SAR imagery revealing the role of the building orientation and the imaging geometry on the building appearance in bistatic SAR imagery.

Future research activities might be addressed to a more comprehensive validation of the model, once bistatic measurements of the target RCS in presence of non-negligible coupling effects will be available. This might be feasible in a near future, once planned bistatic SAR (e.g., Capella bistatic SAR, PLT-1) or polarimetric GNSS-R systems (e.g., HydroGNSS) will be fully operational. Additionally, a more accurate scattering evaluation might be achieved by adopting more refined geometrical models for both the target, e.g., including tilted walls, and the rough surface, e.g., using fractal geometry or including non-linear effects in sea surface, as well as by using more advanced bistatic scattering models, such as two-scale models, SSA.

Author Contributions: Conceptualization, A.D.S. and W.F.; methodology, G.D.M., A.D.S., W.F., A.I., D.R. and G.R.; software, A.D.S. and W.F.; validation, G.D.M., A.D.S., W.F. and A.I.; formal analysis, G.D.M., A.D.S., W.F. and A.I.; investigation, G.D.M., A.D.S., W.F. and A.I.; resources, A.D.S. and W.F.; data curation, A.D.S. and W.F.; writing—original draft preparation, A.D.S. and W.F.; writing—review and editing, G.D.M., A.D.S., W.F., A.I., D.R. and G.R.; supervision, A.I. and D.R.; funding acquisition, G.D.M., A.D.S., A.I., D.R. and G.R. All authors have read and agreed to the published version of the manuscript.

Funding: This work was supported by the Italian Space Agency through the Project "SimulAzione e Modellazione del Sistema BistAtico COSMO-SkyMed/Platino (SAMBA)" (Agreement n. 2023-5-HB.0), CUP n. F63C23000860001.

Institutional Review Board Statement: Not applicable.

Informed Consent Statement: Not applicable.

Data Availability Statement: The original contributions presented in this study are included in the article. Further inquiries can be directed to the corresponding author.

Conflicts of Interest: The authors declare no conflicts of interest.

References

1. Di Simone, A.; Park, H.; Riccio, D.; Camps, A. Sea Target Detection Using Spaceborne GNSS-R Delay-Doppler Maps: Theory and Experimental Proof of Concept Using TDS-1 Data. *IEEE J. Sel. Top. Appl. Earth Obs. Remote Sens.* **2017**, *10*, 4237–4255. [CrossRef]
2. Iervolino, P.; Guida, R. A novel ship detector based on the generalized-likelihood ratio test for SAR imagery. *IEEE J. Sel. Top. Appl. Earth Obs. Remote Sensing* **2017**, *10*, 3616–3630. [CrossRef]
3. Guida, R.; Iodice, A.; Riccio, D. Height retrieval of isolated buildings from single high-resolution SAR images. *IEEE Trans. Geosci. Remote Sens.* **2010**, *48*, 2967–2979. [CrossRef]

4. Iervolino, P.; Guida, R.; Iodice, A.; Riccio, D. Flooding Water Depth Estimation with High-Resolution SAR. *IEEE Trans. Geosci. Remote Sens.* **2015**, *53*, 2295–2307. [CrossRef]
5. Deng, M.; Chen, R.; Chen, Z.; Bu, L.; Zhang, Z.; Wang, C.; Yang, Y. Spaceborne SAR Radiometric Cross-Calibration Considering Typical Scattering Effects in Building Areas. *IEEE Trans. Geosci. Remote Sens.* **2024**, *62*, 1–11. [CrossRef]
6. Renga, A.; Gigantino, A.; Graziano, M.D.; Moccia, A.; Tebaldini, S.; Monti-Guarnieri, A. Bistatic SAR Techniques and Products in a long baseline spaceborne scenario: Application to PLATiNO-1 mission. In Proceedings of the EUSAR 2024, Munich, Germany, 23–26 April 2024.
7. Barrick, D.E. *Radar Cross Section Handbook*; Plenumpress: New York, NY, USA, 1970; Volume II.
8. Ulaby, F.T.; Moore, R.K.; Fung, A.K. *Microwave Remote Sensing*; Artech House: Reading, MA, USA, 1982; Volume II.
9. Tsang, L.; Kong, J.A. *Scattering of Electromagnetic Waves: Advanced Topics*; John Wiley and Sons: New York, NY, USA, 2001.
10. Pino, M.; Rodrìguez, J.; Obelleiro, F. Statistical description of the RCS of 2-D ship models on rough sea surfaces. *Microw. Opt. Technol. Lett.* **2002**, *32*, 153–159. [CrossRef]
11. Pino, M.R.; Landesa, L.; Rodriguez, J.L.; Obelleiro, F.; Burkholder, R.J. The generalized forward-backward method for analyzing the scattering from targets on ocean-like rough surfaces. *IEEE Trans. Antennas Propag.* **1999**, *47*, 961–969. [CrossRef]
12. Ozgun, O.; Kuzuoglu, M. Monte Carlo-Based Characteristic Basis Finite-Element Method (MC-CBFEM) for Numerical Analysis of Scattering from Objects On/Above Rough Sea Surfaces. *IEEE Trans. Geosci. Remote Sens.* **2012**, *50*, 769–783. [CrossRef]
13. Deng, F.S.; He, S.Y.; Chen, H.T.; Hu, W.D.; Yu, W.X.; Zhu, G.Q. Numerical simulation of vector wave scattering from the target and rough surface composite model with 3-D multilevel UV method. *IEEE Trans. Antennas Propag.* **2010**, *58*, 1625–1634. [CrossRef]
14. Liu, P.; Jin, Y.Q. The finite-element method with domain decomposition for electromagnetic bistatic scattering from the comprehensive model of a ship on and a target above a large-scale rough sea surface. *IEEE Trans. Geosci. Remote Sens.* **2004**, *42*, 950–956.
15. Qi, C.; Zhao, Z.; Nie, Z.P. Numerical Approach on Doppler Spectrum Analysis for Moving Targets Above a Time-Evolving Sea Surface. *Prog. Electromagn. Res.* **2013**, *138*, 351–365. [CrossRef]
16. Zhang, M.; Zhao, Y.; Li, J.X.; Wei, P.B. Reliable Approach for Composite Scattering Calculation From Ship Over a Sea Surface Based on FBAM and GO-PO Models. *IEEE Trans. Antennas Propag.* **2017**, *65*, 775–784. [CrossRef]
17. Chen, H.; Zhang, M.; Yin, H.C. Facet-based treatment on microwave bistatic scattering of three-dimensional sea surface with electrically large ship. *Prog. Electromagn. Res.* **2012**, *123*, 385–405. [CrossRef]
18. Man, M.; Lei, Z.; Xie, Y.; Li, X. Bistatic RCS prediction of composite scattering from electrically very large ship-sea geometry with a hybrid facet-based KA and shadow-corrected GRECO scheme. *Prog. Electromagn. Res. B* **2014**, *60*, 35–48. [CrossRef]
19. Gedney, J.J.; Johnson, J.T.; Burkholder, R.J. An Analytical Formulation for the Coherent Scattered Field of a Target Above a Randomly Rough Surface. *IEEE Trans. Antennas Propag.* **2025**, *73*, 329–340. [CrossRef]
20. Franceschetti, G.; Iodice, A.; Riccio, D. A canonical problem in electromagnetic backscattering from buildings. *IEEE Trans. Geosci. Remote Sens.* **2002**, *40*, 1787–1801. [CrossRef]
21. Ferro, A.; Brunner, D.; Bruzzone, L.; Lemoine, G. On the relationship between double bounce and the orientation of buildings in VHR SAR images. *IEEE Geosci. Remote Sens. Lett.* **2011**, *8*, 612–616. [CrossRef]
22. Di Simone, A.; Fuscaldo, W.; Millefiori, L.M.; Riccio, D.; Ruello, G.; Braca, P.; Willett, P. Analytical Models for the Electromagnetic Scattering from Isolated Targets in Bistatic Configuration: Geometrical Optics Solution. *IEEE Trans. Geosci. Remote Sens.* **2020**, *58*, 861–880. [CrossRef]
23. Di Martino, G.; Di Simone, A.; Fuscaldo, W.; Iodice, A.; Riccio, D.; Ruello, G. Electromagnetic Scattering from a Canonical Target over an Anisotropic Rough Surface using Geometrical Optics. In Proceedings of the 2020 XXXIIIrd General Assembly and Scientific Symposium of the International Union of Radio Science, Rome, Italy, 29 August–5 September 2020; pp. 1–4.
24. Fuscaldo, W.; Di Simone, A.; Millefiori, L.M.; Iodice, A.; Braca, P.; Willett, P. A Convenient Analytical Framework for Electromagnetic Scattering from Composite Targets. *Radio Sci.* **2019**, *54*, 785–807. [CrossRef]
25. Fung, A.K. *Microwave Scattering and Emission Models and Their Application*; Artech House: Boston, MA, USA, 1994.
26. Ticconi, F.; Pulvirenti, L.; Pierdicca, N. *Models for Scattering from Rough Surfaces*; IntechOpen: London, UK, 2011; pp. 203–226.
27. Franceschetti, G.; lodice, A.; Riccio, D. Chapter 1.6.5-Fractal Models for Scattering from Natural Surfaces. In *Scattering*; Pike, R., Sabatier, P., Eds.; Academic Press: London, UK, 2002; pp. 467–485. [CrossRef]
28. Fois, F. Enhanced Ocean Scatterometry. Ph.D. Thesis, Technische Universiteit Delft, Delft, The Netherlands, 2015.
29. Nouguier, F.; Guérin, C.A.; Chapron, B. "Choppy wave" model for nonlinear gravity waves. *J. Geophys. Res. Ocean.* **2009**, *114* . [CrossRef]
30. Bussey, H.E.; Gray, J.E.; Bamberger, E.C.; Rushton, E.; Russell, G.; Petley, B.W.; Morris, D. International Comparison of Dielectric Measurements. *IEEE Trans. Instrum. Meas.* **1964**, *IM-13*, 305–311. [CrossRef]
31. Eigel, R.L.; Collins, P.J.; Terzuoli, A.J.; Nesti, G.; Fortuny, J. Bistatic scattering characterization of complex objects. *IEEE Trans. Geosci. Remote Sens.* **2000**, *38*, 2078–2092. [CrossRef]

32. Bender, C.M.; Orszag, S.A. *Advanced Mathematical Methods for Scientists and Engineers: Asymptotic Methods and Perturbation Theory*; Springer: Berlin/Heidelberg, Germany, 1999; Volume 1.
33. Johnson, J. A numerical study of scattering from an object above a rough surface. *IEEE Trans. Antennas Propag.* **2002**, *50*, 1361–1367. [CrossRef]
34. Quiney, R.G.; Austin, F.R.; Sargent, L.B., Jr. The Measurement of Surface Roughness and Profiles on Metals. *ASLE Trans.* **1967**, *10*, 193–202. [CrossRef]
35. Beckmann, P.; Spizzichino, A. *The Scattering of Electromagnetic Waves from Rough Surfaces*; Artech House: Norwood, MA, USA, 1963.
36. Tsang, L.; Kong, J.A.; Shin, R. *Theory of Microwave Remote Sensing*; Wiley: New York, NY, USA, 1985.
37. Di Martino, G.; Di Simone, A.; Iodice, A.; Riccio, D.; Ruello, G. Cardinal Effect in Bistatic SAR Imagery: Analysis and Physical Interpretation. In Proceedings of the IGARSS 2024-2024 IEEE International Geoscience and Remote Sensing Symposium, Athens, Greece, 7–12 July 2024; pp. 10944–10947.